Histone degradation in response to DNA damage enhances chromatin dynamics and recombination rates

Hauer, Michael H.; Seeber, Andrew; Singh, Vijender; Thierry, Raphael; Sack, Ragna; Amitai, Assaf

Published in:
Nature Structural & Molecular Biology

DOI:
10.1038/nsmb.3347

Publication date:
2017

Document Version
Peer reviewed version

Histone degradation in response to DNA damage enhances chromatin dynamics and recombination rates

Michael H. Hauer[1,2], Andrew Seeber[1,2], Vijender Singh[3], Raphael Thierry[1], Ragna Sack[1], Assaf Amitai[4,+], Mariya Kryzhanovska[1], Jan Eglinger[1], David Holcman[4], Tom Owen-Hughes[3] and Susan M. Gasser[1,2,*]

Institutions

1) Friedrich Miescher Institute for Biomedical Research, Maulbeerstr. 66, CH-4058 Basel, Switzerland
2) University of Basel, Faculty of Natural Sciences, CH-4056 Basel, Switzerland
3) Centre for Gene Regulation and Expression, School of Life Sciences, University of Dundee, Dundee DD1 5EH, UK
4) Institut de Biologie de l'École Normale Supérieure, Ecole Normale Supérieure, 46 rue d'Ulm 75005 Paris, France

Present addresses

+ Institute for Medical Engineering & Science, The Massachusetts Institute of Technology, Cambridge, Massachusetts

Corresponding author statement

*Correspondence should be addressed to S.M.G.: susan.gasser@fmi.ch

Abstract

Nucleosomes are essential for proper chromatin organization and the maintenance of genome integrity. Histones are post-translationally modified and often evicted at sites of DNA breaks, facilitating recruitment of repair factors. Whether such chromatin changes are localized or genome-wide is debated. Here we show that cellular levels of histones drop 20-40% in response to DNA damage. This histone-loss occurs from chromatin, is proteasome mediated and requires both the DNA damage checkpoint and INO80 nucleosome remodeler. Histone level reduction was confirmed by SILAC-based mass spectroscopy, genome-wide nucleosome mapping and fluorescence microscopy. Chromatin decompaction and increased fiber flexibility accompany histone degradation, both in response to DNA damage and upon artificially reducing histone levels. As a result, recombination rates and DNA repair focus turnover are enhanced. Thus, we propose that a generalized reduction in nucleosome occupancy is an integral part of the DNA damage response, providing mechanisms for enhanced chromatin mobility and homology search.

-------- 150 words ---------

Introduction

The genomic DNA of eukaryotes is highly organized and packed into chromatin. The most basic unit of chromatin is the nucleosome which is formed by 146 base base pairs of DNA that wrap around an octameric core of histone proteins. Chromatin remodelers use the energy from ATP hydrolysis to change the local state of chromatin by sliding/spacing or ejecting nucleosomes. These actions regulate gene transcription[1], replication[2], chromatin structure and DNA repair genome-wide[3,4]. Cellular genomes are constantly exposed to different sources of DNA damage, requiring that the repair machinery both disrupts and restores chromatin structure[5]. Heterochromatic chromatin tends to obstruct repair protein access and DNA double-strand breaks (DSB) found in heterochromatin relocate to the edge of such domains[6-8], a phenomenon that requires a certain degree of physical mobility.

In budding yeast and human cells exposed to DNA damage, increases in chromatin mobility were observed both at lesions[9-11] and at undamaged sites where no DSB could be detected[10,12]. The chromatin remodeler INO80-C and activation of the DNA damage checkpoint (DDC) were implicated in both processes[9,10,12]. Functionally, enhanced local DSB mobility correlated with efficient repair by homologous recombination (HR)[9]. Modelling algorithms (Amitai A., Seeber A. *et al.*, ***in preparation***) suggest that mobility could enhance the search for the donor sequence required for homology-based repair. Consistently, elevated chromatin mobility was shown to result in genomic translocations in human cells[11]. However, the mechanisms that underlie enhanced chromatin mobility have remained elusive. Here we show that nucleosome degradation triggered by remodelers and checkpoint proteins enhances chromatin movement and accessibility, and promotes efficient repair.

Results

DNA damage triggers extensive histone loss from chromatin

To investigate whether DNA damage and DDC activation affect chromatin structure and/or composition genome-wide, we used quantitative SILAC mass spectrometry in *Saccharomyces cerevisiae* and measured histone abundance before and after acute treatment (1 hour) with the radiomimetic drug Zeocin. Relative ratios of non-modified histone peptides (damage over control - L/H) indicate a substantial loss of 20±6 % of all core histones H2A, H2B, H3 and H4 (**Fig. 1a**, **Supplementary Fig. 1a-f**). Interestingly, levels of the histone variant Htz1 (H2A.Z) remained rather stable. Quantitative immunoblot analysis confirmed our observations and showed robust DDC activation (γH2A signal, Rad53 upshift) along with a dose-dependent relationship between histone H3/H4 loss and Zeocin treatment (**Fig. 1b**). The same effect was observed using another source of DNA damage, ionizing radiation (γ-IR) (**Supplementary Fig. 2a-d**).

Despite being highly quantitative for protein abundance, mass spectrometry data does not distinguish between histone pools and nucleosomes, and it lacks positional information. To investigate whether entire nucleosomes were lost globally following DNA damage or at specific genomic loci, we performed genome-wide nucleosome mapping. First, we found that the positioning of nucleosomes around the promoters of yeast genes changed little following damage induction (**Fig. 1c**). To assess global changes in nucleosome abundance, we implemented internal standardization by mixing defined numbers of *Candida glabrata* cells with the experimental *Saccharomyces cerevisiae* cells prior to chromatin preparations[13]. Normalization of the *S. cerevisiae* reads with respect to the *C. glabrata* reads showed that there was a drop in nucleosome occupancy both within promoters and across coding regions following Zeocin treatment (**Fig. 1c and Supplementary Table 1)**. This effect was just as strong on a subset of 750 low expression genes (**Fig. 1c**) as on highly transcribed genes (**Supplementary Fig. 2e**), suggesting that transcription is unlikely to regulate or drive the reduction. Finally, we found no preferential depletion specific structural elements such as centromeres or telomeres, arguing that the effect is widespread.

To determine the kinetics of histone reduction, we used time-lapse live cell tracking of functional fluorescently labeled ectopic histone H2B (H2B-CFP) or control Htz1-mEos and Nup49-GFP, which labels the nuclear rim (**Fig. 1d**, **Supplementary Fig. 2g**, **Supplementary Video 1**)**.** We used microfluidic chambers to trap cells and pulse-treated them for 1h with Zeocin, generating roughly 4-7 DSBs per genome[14]. Histone H2B degradation (20±1.7% compared to undamaged cells) occurred within 30 minutes of Zeocin exposure. Neither Nup49-GFP (**Supplementary Fig. 2f**) nor the Htz1-mEos control showed differential loss following DNA damage, suggesting that the induced histone degradation only targets core histones (**Fig. 1d**). Combined with our mass-spectroscopy and immunoblot data, these results suggested a rapid degradation of histones, rather than simply eviction from chromatin. Earlier, Gunjan *et al.* had shown that an excess of nonchromatin-bound histones is phosphorylated by the Rad53 checkpoint kinase, and then subsequently ubiquitinated and subject to proteasomal degradation[15,16]. This prompted us to test whether the proteasome inhibitor MG132 or mutation of the 26S proteasome (*pre1-1, pre2-2*)[17] would suppress the loss of histones from chromatin. Consistent with proteasome involvement, both the inhibitor and the mutations in *PRE1* and *PRE2* genes suppressed the DNA damage-induced H3 or H4 degradation (**Fig. 2**). Moreover, by synchronizing cells in G1, or releasing them into S phase prior to damage, we found that degradation occurs in both phases of the cell cycle (**Supplementary Fig. 3**).

We considered that the observed histone loss might be accentuated by impaired expression of histone genes, which are tightly regulated and show promoter-dependent upregulation in S phase. To eliminate this confounding factor, we placed the H3 and H4 genes under the control of the galactose promoter in a strain in which both endogenous H3 and H4 copies were deleted (histone-shutdown strain, **Supplementary Fig. 4a**). With constitutive H3/H4 expression (growth in media with low level galactose), we found the same depletion effect following exposure to Zeocin as in cells with endogenous histone genes, arguing that DNA damage induces an active degradation of histones, and not simply a loss of new histone synthesis (**Supplementary Fig. 4**). The loss of histones is rapid and so substantial that by 1h, every third nucleosome could be removed from DNA. It is therefore likely that higher-order chromatin structure changes in response to DNA damage.

Damaged chromatin increases mobility, decompaction and flexibility

The increase in chromatin movement following DNA damage has been well documented, although the mechanisms leading to enhanced mobility remained elusive[12,18,19]. To see if histone loss might be at the root of this phenomenon, we examined the physical characteristics of yeast chromatin under the same conditions that triggered histone loss. Using improved imaging protocols, we monitored the volume of chromatin domains in three-dimensional (3D) space, the inherent flexibility of the nucleosome polymer and the physical movement of fluorescently tagged sites.

Previous studies in which chromatin mobility was quantified used low sampling rates during live cell imaging (Δt=1.5 sec) to determine the trajectory of a moving locus and the area explored (radius of constraint)[9-12,20]. However, such low time-resolved data yields little information on chromatin fiber compaction or flexibility. To resolve this, we used a novel high-speed imaging technique (300 ms or 80 ms imaging intervals) with which we first confirmed that increased chromatin mobility can be monitored at a non-damaged site (*MET10*) in cells responding to widespread DNA damage (**Fig. 3a, Supplementary Fig. 5a**). By applying an analysis based on polymer models to our high-speed imaging data (Amitai A., Seeber A. *et al., **in preparation***), we estimated biophysical parameters that predict both the expansion of chromatin (reflected by an increase in the anomalous exponent α) and the loss of constraining forces that limit chromatin movement (as seen by decrease in the spring constant K_C) (**Fig. 3b and Supplementary Fig. 5b**).

To examine whether the 3D volume of a defined chromatin domain was altered within the nucleus, we used super-resolution microscopy coupled with subsequent machine-learning and 3D pixel classification analysis. Using this technique, we measured the change in volume of TetR-mCherry tagged chromosomal loci (chromatin expansion) in cells fixed 30 min after exposure to different amounts of Zeocin (**Fig. 3c**). Indeed, we scored a dose-dependent decompaction of S phase chromatin: 3D TetR-mCherry foci volumes expanded with increased amounts of damage (**Fig. 3d**).

The second prediction from the polymer modeling of locus dynamics was that the flexibility of the chromatin fiber would be enhanced after DNA damage. Thus, we monitored chromatin flexibility with confocal microscopy and measured the 3D distances between two differentially labeled genomic

loci positioned on the same chromosome arm. We used two independent sets of loci spaced at genomic distances of either 320 kbp on Chr XIV or 50 kbp on Chr III. For the first set, we synchronized cells, fixed them before or after Zeocin treatment and calculated the average of all distances measured between the lacI-GFP and TetR-mRFP fluorescently tagged loci (**Fig. 4a**). We find that after DNA damage, the average inter-spot distance increases significantly both in G1- (0.97-1.2 μm) and S-phase cells (0.99-1.12μm). For the second set of data, a similar approach was taken but we measured the inter-distance between CFP-lacI and TetR-mRFP tagged foci on Chr III in real time (**Supplementary Video 2**). In all cases we included Rad52-GFP and ensured that there was no overlap of Rad52-GFP with either of the other two fluorescent signals, assuring that the measured changes do not arise from effects linked to local DNA repair events. Analysis of relative mean squared distance changes and the average of all measured inter-distances reveals a robust increase in inter-spot dynamics and distances following Zeocin treatment (**Fig. 4b**). These data are consistent with a model in which damage-triggered histone degradation reduces the amount of nucleosomal constraints within the chromatin fiber, causing chromatin to expand. The enhanced physical dynamics would be a reflection of increased flexibility.

Histone abundance dictates chromatin movement and decompaction

To confirm that increased chromatin mobility and decompaction arise as a consequence of histone loss, we made use of a histone-shutdown strain that expresses H3 and H4 under the control of the *GAL1-10* promoter which is susceptible to media-controlled repression as well as induction (**Fig. 5a**). After 1h in galactose, we released α-factor arrested cells bearing this shutdown construct into raffinose-containing medium. Depending on the concentration of raffinose, we observed reduced *GAL1-10*-driven expression, lowering histone levels in a controlled manner by 39% within an hour (**Supplementary Fig. 6ab**). This artificial reduction of histones did not cause DNA damage checkpoint activation, even when levels were reduced extensively (**Supplementary Fig. 6b**). Using the appropriate galactose:raffinose mixture, however, we could reduce histone levels in a controlled manner, even in the absence of damage (**Fig. 5b)**, after which we monitored both chromatin decompaction (**Fig. 5c**) and a striking increase of chromatin mobility, measured at the *MGS1* locus after 1h on the defined medium (**Fig. 5d**).

To further validate these findings, we made use of a mutant bearing deletions of both high-mobility group protein one (HMGB1) orthologues *NHP6A* and *NHP6B* (*nhp6a*Δ*nhp6b*Δ, for simplicity

called *nhp6*Δ), which was previously described as having reduced levels of core histone proteins[21]. Here, we show that *nhp6*Δ does not trigger endogenous damage checkpoints, and has neither an altered FACS distribution (**Fig. 6b**) nor Rad53 activation (**Supplementary Fig. 7a**), yet by tracking chromatin mobility with the high-speed imaging regime we find that the mobility of two labeled foci, *MET10* and *PES4*, is significantly enhanced in *nhp6*Δ cells (**Fig. 6cd, Supplementary Fig. 7b**). High resolution time-lapse imaging of the GFP-LacI-tagged *PES4* or the TetR-mCherry-tagged *MET10* locus further confirms an increase in chromatin flexibility which is reflected by a decrease in the spring constant K_C, and a positive trend in the anomalous exponent α (**Fig. 6e, Supplementary Fig. 7cd**). Finally, using super-resolution microscopy we monitored an increase in 3D volume of the TetR-mCherry labeled *MET10* locus in *nhp6*Δ cells, which was more pronounced in an asynchronous culture, for unknown reasons (**Fig. 6f**). Combined with the effects observed in the histone shutdown strain, these manipulations argue for a direct link between histone levels and chromatin movement.

Histone loss is checkpoint and INO80-C dependent and modulates recombination efficiency

DNA damage activates the central DDC kinase Mec1 (ATR) which initiates a widespread phosphorylation cascade leading to a global damage response and cell-cycle arrest. Additionally, repair proteins such as Mre11, Exo1, Rad51 and Rad52 act locally on DNA to mediate resection and preparation for either repair by homologous recombination or end-joining. Among Mec1 targets are the downstream effector kinase Rad53 (CHK2)[22] and multiple subunits of the INO80-C remodeler[23,24]. Since both INO80-C and DDC proteins were implicated in a general increase in chromatin mobility in response to DNA damage[12], we hypothesized that these factors may also regulate histone loss, which we find can trigger enhanced chromatin mobility.

Using immunoblotting, we found that strains lacking checkpoint kinases Mec1 or Rad53 completely abolished histone degradation after Zeocin treatment (**Fig. 7ab**). More strikingly, the same dependency was observed for strains deleted for INO80-C subunits Arp8, Ies4 or Arp5 which do not participate in the DDC, but remodel nucleosomes (**Fig. 7ab**). Importantly, histone loss occurred independently of Rad51 and Exo1 showing that local repair events are not necessary for the DDC-triggered degradation of histones. We further confirmed this with two other assays: H2B-CFP fluorescence monitoring over time (**Fig. 7c**) and super-resolution microscopy of tagged locus 3D

volumes (**Fig. 7d**). In all cases we find that histone loss and chromatin expansion required the Mec1-mediated checkpoint and intact INO80-C: no histone loss or chromatin expansion is seen in *mec1*Δ*sml1*Δ and *rad53*Δ nor in *arp8*Δ), while cells bearing *sml1*Δ (a control for the *mec1*Δ*sml1*Δ) and *rad51*Δ behaved like their wild-type counterparts in response to damage (**Fig. 7c-d**).

The main role of the DDC kinase Mec1/ATR is to trigger a cell-wide stress response that helps the cell cope with DNA damage. This appears to be, at least in part, mediated by the remodeler INO80-C[23,24]. The importance of chromatin-remodeling in histone degradation, is not entirely surprising, given that Ino80 was recently shown to interact with Cdc48, an AAA^+ ATPase involved in proteasome-dependent protein degradation[25]. Moreover, both Mec1 and INO80-C are linked to RNA Pol II eviction at sites of replication fork-transcription collision[24]. Thus, these genetic dependencies further validate our model that histone degradation and chromatin expansion are the key phenomena underlying damage-enhanced chromatin movement (**Fig. 7e**). Our data further suggest that a failure to degrade histones might impair the access of repair proteins to chromatin, giving an explanation for previously observed repair deficiencies in these mutants[26,27].

To examine the functional relevance of the observed reduction in nucleosome occupancy triggered by DNA damage, and to test the hypothesis that nucleosome reduction facilitates homologous recombination and thus DNA repair, we made use of a recombination assay that monitors the integration rates of two different *URA3* cassettes (800 bp homology or 82 bp homology) at two independent loci (*MGS1* and *URA3*). In otherwise isogenic haploid strains, we impaired INO80-C activity by disrupting its nucleosome-binding subunit Arp8 (*arp8*Δ) or deleted both *NHP6* genes, to reduce nucleosome levels genome-wide[21]. Consistent with previously reported recombination defects in *arp8*Δ[26,27], we see reduced recombination rates in this mutant, while rates were significantly increased in the *nhp6*Δ strain (**Fig. 8a**). Interestingly, Liang *et al.* had shown that deletion of the histone H3-H4 gene copy 2 (HHT2-HHF2) can confer resistance to DNA damaging agents and restore the viability of DDC mutants under stress conditions[16]. Thus, we hypothesized that artificially lowering histone levels by Nhp6 removal might rescue *arp8*Δ sensitivity and even increase the fitness of wild-type cells under damaging conditions. Using a recovery assay that scores cell survival after a 1h treatment with increasing amounts of Zeocin, we found that *nhp6*Δ cells recover better from acute DNA damage than a wild-type strain, and that

lowering nucleosome occupancy by deleting *NHP6* partially rescues the Zeocin sensitivity of an *arp8*Δ strain (**Fig. 8b**).

The observation that increased recombination rates in *nhp6*Δ cells stem from changes in nucleosome occupancy, prompted us to test whether gene targeting rates could also be increased by other approaches that reduce histone levels. Hence, we used the same recombination assay in our histone-shutdown strain and followed the integration of two different hygromycin-resistance markers either at *ATG2* or *MGS1*. This was done directly after a 2h incubation in raffinose-containing medium (raffinose only or a defined 1:20 galactose:raffinose mixture) which reduces histone H3 and H4 levels (**Fig. 8c**). Consistent with the *nhp6*Δ experiment, we found that a reduction of histone levels by means of transcriptional repression significantly enhances the integration rates of both *ATG2::hygro* and *MGS1::hygro* PCR products (**Fig. 8d**).

Finally, we used fluorescence microscopy to follow the kinetics of Rad52-GFP focus formation and dissolution during 16h after a brief exposure to Zeocin. We find fewer Rad52 (BRCA2) foci in *nhp6*Δ *vs* wild-type cells (**Supplementary Fig. 7e**). Since Rad52 accumulates at sites of damage and disappears upon completion of recombination mediated repair[28], this result suggests that a reduction in histone levels enhances the turnover of the recombination-mediated repair reaction.

Discussion

In a robust combinatorial approach, we used quantitative mass spectrometry, fluorescent live cell microscopy and genome-wide nucleosome mapping to show that core histone proteins but not histone variant Htz1 are degraded from chromatin when the genome is challenged with DNA damage. This requires checkpoint activation, INO80-C function and is mediated through the proteasome. Furthermore, reducing the levels of histones on DNA enhances chromatin mobility, decompaction and fiber flexibility. Proteins that function uniquely in recombination-mediated DNA repair (Rad51, Exo1) were not involved in histone loss, while the Mec1-target INO80-C, a chromatin remodeler implicated in efficient repair, is. Other studies have postulated a release of chromosomal tethers around the centromere as the source for altered chromatin mobility[20,29]. This, however, is unable to account for the observed

expansion of non-centromeric chromatin nor for the observed dependence on INO80-C for these events. Furthermore, there is no evidence to date that centromeres delocalize in response to damage.

While we cannot rule out that other mechanisms also contribute to nuclear or chromosomal motion, our data irrefutably demonstrate that a reduction of histone levels, even in the absence of DNA damage, is sufficient to decompact chromatin and enhance chromatin mobility. We suggest that histone degradation facilitates the search for donor sequences, an event required for DSB repair by homologous recombination with a non-sister template, and that chromatin decompaction might further enhance the access of DNA (both damage and template) to the repair machinery. On the other hand, mobility might also help disrupt improper pairing events during HR. Recombination assays indicate that a reduction in nucleosome occupancy by *NHP6* deletion cells or by means of transcriptional histone gene repression increases gene targeting rates and enhances the turnover rate of repair processes. While controlled histone loss might facilitate repair, its misregulation and the resulting effects in chromatin structure and dynamics are likely to promote oncogenic translocations that might drive tumorigenesis.

Taken together, our study identifies histone loss as a fairly immediate response to DNA damage checkpoint activation and implicates remodeler-dependent histone degradation as a novel and integral part of the DNA damage response. We demonstrate how changes in chromatin composition can affect the physical characteristics of chromatin and we show that artificial histone level reduction can be used to increase recombination efficiency. To understand how the posttranslational modification status of histones and the entire chromatin proteome changes upon DNA damage requires further investigation. We speculate that gene targeting rates in mammalian cells can also be improved by manipulating histone occupancy.

Acknowledgements

M.H.H. thanks Shany Koren-Hauer for critical reading and assistance in preparing the manuscript and Vincent Dion and Helder Ferreira for fruitful discussions and advice. We thank Vincent Dion (strain GA-5816), James Haber (strain JKM-179); Brian Luke (strain GA-3364), Kerstin Bystricky (precursor strain for GA-9777, strain GA-9227), Jean-Marc Galan (strain GA-1364, GA-1365, GA-1366) and Fred Winston (plasmids #3494, #3495) for reagents and material. We are grateful for the technical assistance provided by Laurent Gelman (microscopy), Steven Bourke (microscopy) and Hubertus Kohler (FACS). M.H.H. thanks the Bioinformatics facility for help in getting started with R. We thank all members of the FMI Protein Analysis and Microscopy facilities for valuable advice and support. We thank all members from the Gasser laboratory for valuable discussions and technical support. M.H.H. was supported by a PhD fellowship of the Boehringer Ingelheim Fonds. S.M.G. thanks the HFSP, SNSF and the Novartis Research Foundation for support.

Author contributions

M.H.H. and S.M.G wrote the manuscript. M.H.H. designed experiments and analyzed the data. M.H.H. performed most of the experiments. A.S. contributed to experimental design, data analysis, the manuscript and performed high-speed live cell tracking upon Zeocin treatment. M.H.H. planned and M.H.H. and A.S. performed the ectopic integration assays and the Rad52-YFP recovery assay. M.K. assisted in ectopic recombination assays. V.S. and T.O.-H. performed and analyzed genome-wide nucleosome mapping. A.A. and D.H. performed biophysical analysis of high-speed tracking data. R.T. performed and maintained the coding for 3D SIM-data analysis. R.S. performed all mass spectrometry measurements and the analysis of label-free experiments. J.E. performed and maintained the coding of tools for 3D inter-distance measurements. All the authors discussed the data and participated in the preparation of the manuscript.

Competing Financial Interests

The authors declare no competing financial interests.

References (main text only)

1. Boettiger, A.N. et al. Super-resolution imaging reveals distinct chromatin folding for different epigenetic states. *Nature* **529**, 418-22 (2016).
2. Aze, A., Sannino, V., Soffientini, P., Bachi, A. & Costanzo, V. Centromeric DNA replication reconstitution reveals DNA loops and ATR checkpoint suppression. *Nat Cell Biol* **18**, 684-91 (2016).
3. Gerhold, C.B., Hauer, M.H. & Gasser, S.M. INO80-C and SWR-C: guardians of the genome. *J Mol Biol* **427**, 637-51 (2015).
4. Seeber, A., Hauer, M. & Gasser, S.M. Nucleosome remodelers in double-strand break repair. *Curr Opin Genet Dev* **23**, 174-84 (2013).
5. Soria, G., Polo, S.E. & Almouzni, G. Prime, repair, restore: the active role of chromatin in the DNA damage response. *Mol Cell* **46**, 722-34 (2012).
6. Chiolo, I. et al. Double-Strand Breaks in Heterochromatin Move Outside of a Dynamic HP1a Domain to Complete Recombinational Repair. *Cell* **144**, 732-744 (2011).
7. Lemaitre, C. et al. Nuclear position dictates DNA repair pathway choice. *Genes Dev* **28**, 2450-63 (2014).
8. Torres-Rosell, J. et al. The Smc5-Smc6 complex and SUMO modification of Rad52 regulates recombinational repair at the ribosomal gene locus. *Nat Cell Biol* **9**, 923-31 (2007).
9. Dion, V., Kalck, V., Horigome, C., Towbin, B.D. & Gasser, S.M. Increased mobility of double-strand breaks requires Mec1, Rad9 and the homologous recombination machinery. *Nat Cell Biol* **14**, 502-9 (2012).
10. Mine-Hattab, J. & Rothstein, R. Increased chromosome mobility facilitates homology search during recombination. *Nat Cell Biol* **14**, 510-7 (2012).
11. Roukos, V. et al. Spatial dynamics of chromosome translocations in living cells. *Science* **341**, 660-4 (2013).
12. Seeber, A., Dion, V. & Gasser, S.M. Checkpoint kinases and the INO80 nucleosome remodeling complex enhance global chromatin mobility in response to DNA damage. *Genes Dev* **27**, 1999-2008 (2013).
13. Hu, B. et al. Biological chromodynamics: a general method for measuring protein occupancy across the genome by calibrating ChIP-seq. *Nucleic Acids Res* **43**, e132 (2015).
14. Povirk, L.F., Wubter, W., Kohnlein, W. & Hutchinson, F. DNA double-strand breaks and alkali-labile bonds produced by bleomycin. *Nucleic Acids Res* **4**, 3573-80 (1977).
15. Gunjan, A. & Verreault, A. A Rad53 kinase-dependent surveillance mechanism that regulates histone protein levels in S. cerevisiae. *Cell* **115**, 537-49 (2003).
16. Liang, D., Burkhart, S.L., Singh, R.K., Kabbaj, M.H. & Gunjan, A. Histone dosage regulates DNA damage sensitivity in a checkpoint-independent manner by the homologous recombination pathway. *Nucleic Acids Res* **40**, 9604-20 (2012).

17. Heinemeyer, W., Kleinschmidt, J.A., Saidowsky, J., Escher, C. & Wolf, D.H. Proteinase yscE, the yeast proteasome/multicatalytic-multifunctional proteinase: mutants unravel its function in stress induced proteolysis and uncover its necessity for cell survival. *EMBO J* **10**, 555-62 (1991).

18. Dion, V. & Gasser, S.M. Chromatin movement in the maintenance of genome stability. *Cell* **152**, 1355-64 (2013).

19. Krawczyk, P.M. et al. Chromatin mobility is increased at sites of DNA double-strand breaks. *Journal of Cell Science* **125**, 2127-2133 (2012).

20. Strecker, J. et al. DNA damage signalling targets the kinetochore to promote chromatin mobility. *Nat Cell Biol* **18**, 281-90 (2016).

21. Celona, B. et al. Substantial histone reduction modulates genomewide nucleosomal occupancy and global transcriptional output. *PLoS Biol* **9**, e1001086 (2011).

22. Sanchez, Y. et al. Regulation of RAD53 by the ATM-like kinases MEC1 and TEL1 in yeast cell cycle checkpoint pathways. *Science* **271**, 357-60 (1996).

23. Morrison, A.J. et al. Mec1/Tel1 phosphorylation of the INO80 chromatin remodeling complex influences DNA damage checkpoint responses. *Cell* **130**, 499-511 (2007).

24. Poli, J. et al. Mec1, INO80, and the PAF1 complex cooperate to limit transcription replication conflicts through RNAPII removal during replication stress. *Genes Dev* **30**, 337-54 (2016).

25. Lafon, A. et al. INO80 Chromatin Remodeler Facilitates Release of RNA Polymerase II from Chromatin for Ubiquitin-Mediated Proteasomal Degradation. *Mol Cell* **60**, 784-96 (2015).

26. Chen, X. et al. The Fun30 nucleosome remodeller promotes resection of DNA double-strand break ends. *Nature* **489**, 576-80 (2012).

27. van Attikum, H., Fritsch, O. & Gasser, S.M. Distinct roles for SWR1 and INO80 chromatin remodeling complexes at chromosomal double-strand breaks. *Embo j* **26**, 4113-25 (2007).

28. Lisby, M., Barlow, J.H., Burgess, R.C. & Rothstein, R. Choreography of the DNA damage response: spatiotemporal relationships among checkpoint and repair proteins. *Cell* **118**, 699-713 (2004).

29. Verdaasdonk, J.S. et al. Centromere tethering confines chromosome domains. *Mol Cell* **52**, 819-31 (2013).

Figure legends

Figure 1: DNA damage triggers a global loss of core histones from chromatin

Damage-dependent global histone degradation quantified by (**a)** SILAC mass spectrometry on chromatin fractions from two independent cells pools (for further information see **Supplementary Fig. 1**). Boxplots show light/heavy histone peptide distribution indicating the degradation of core histones and, to a lesser extent, Htz1 (H2A.Z). (**b)** Right: Representative immunoblot analysis using antibodies against H3 and H4 on whole cell extracts from asynchronous (asy.) wild-type cultures in response to Zeocin treatment. Rad53 and γH2A were probed to confirm checkpoint activation. MCM2 was used to control for loading and Ctr. represents bands on the Ponceau stained membrane. Left: Schematic illustrates the experimental setup and bar graph shows mean values of immunoblot quantification of H3 and H4 blots from at least four independent experiments upon Zeocin treatment relative to the control condition. Asterisk indicates phosphorylation-dependent Rad53 mobility shift. (**c**) Genome-wide nucleosome mapping. Scheme illustrates the effect of histone loss on nucleosome reads. Graphs show the distribution of nucleosome reads over all genes and over the bottom 10% of low level expressed genes aligned to the TSS from four independent experiments (±s.d. is shaded). (**d**) Live single-cell microscopy of H2B-CFP and Htz1-mEos. Graphs show the experimental outline, representative images and the mean fluorescent signals of all individual cells (cell numbers indicated in graph) per treatment over time relative to the control (Ctr.) condition. Scale bar is 2 μm. Uncropped blot images are shown in **Supplementary Dataset 1**. Boxplots in **a** represent median values, interquartile ranges and whiskers. Graphs in **b**,**d** show means ± s.e.m, in **c** ± s.d..

Figure 2: Histones are degraded by the proteasome

(**a**) Scheme illustrates the experimental setup. (**a-b)** Immunoblot analysis and quantification showing H3 or H4 levels before and after Zeocin treatment in whole cell extracts from asynchronously (Asy.) growing wild-type cells (**a**, experiment was done in triplicate) or *erg6*Δ cells (**b**, experiment was done in triplicate) treated with the proteasome inhibitor MG132. MG132 permeability is increased in *erg6*Δ cells which rescues histone H3 from being degraded. Antibodies against ubiquitin (Ubi) indicate proper

function of the MG132 inhibitor validating the experimental protocol. (**c**) Immunoblot analysis and quantification showing H4 levels in response to Zeocin treatment in wild-type and 26S proteasome dysfunctional cells (*pre1-1*, *pre2-2*) (experiment was done in four replicates). Mutations in *PRE1* and *PRE2* suppress histone H4 degradation. Rad53 and γH2A were probed to confirm checkpoint activation. Ctr. shows loading and represents bands on the original gel (UV-TGX stained). Uncropped blot images are shown in **Supplementary Dataset 1**. Bar graphs show means ± s.e.m.. Asterisk indicates Phosphorylation-dependent Rad53 mobility shift.

Figure 3: High-speed, live cell imaging and super-resolution microscopy shows chromatin expansion and enhanced flexibility following DNA damage

(a) Diagram with representative image shows the experimental setup for high-speed imaging. Graph shows MSD analysis (Δt=300 ms) of the *MET10* locus in response to Zeocin treatment indicating a dose-dependent increases in global chromatin mobility in response to DNA damage ($n^{Ctr.}$=23, n^{Zeo200}=15, n^{Zeo500}=21 different cells from three independent experiments). Scale bar is 2 µm. **(b)** Graphs show the medians and whiskers of biophysical parameters derived from imaging data and predict chromatin expansion and flexibility increases after Zeocin treatment. (**c**) Experimental outline and FACS analysis of cell cycle stages. (**d**) Scheme illustrates the 3D super-resolution imaging regime. Boxplots showing TetR-mCherry focus volume distributions upon Zeocin treatment in S phase cells relative to the control (Ctr.) condition of multiple single cells (n numbers in graph) from two different cultures. All MSD graphs represent the mean ± s.e.m. of cells pooled from three independent experiments. Boxplots in **d** represent median values, interquartile ranges and whiskers. P-values, *P<0.05, **P<0.01, ***P<0.001, result from unequal variances t-tests for **d** or Kolmogorow-Smirnow-Tests for **b**. Additionally, consult **Supplementary Dataset 2** for mobility parameters and the number of cells analyzed.

Figure 4: DNA damage increases chromatin flexibility

(a) Upper panel illustrates the experimental setup and procedure for 3D intra-chromosomal distance measurements between two tagged loci on Chr XIV. Boxplots and cumulative distribution graphs in lower panel show GFP to mRFP distance distributions from multiple single cells (n numbers in graph) from two different cultures in fixed condition before and after Zeocin treatment in G1 phase or after release into S phase. (**b**) Upper panel illustrates live cell imaging regime used to monitor distance changes between two loci on the left arm of Chr III over time and upon Zeocin treatment. Exemplary tracks indicate the movement of CFP and mRFP foci over time. Relative MSD graph in lower panel shows mean values ± s.e.m from multiple single ($n^{Ctr.}$=13, n^{Zeo}=53) cells from two different cultures and indicates less constrained spot movement upon DNA damage. Boxplots represent median values, interquartile ranges and whiskers and show the distribution of all measured CFP to mRFP distances. P-values, *P<0.05, ***P<0.001, NS=not significant, result from unequal variances t-tests.

Figure 5: Artificial histone reduction in the absence of damage triggers chromatin expansion and increased motion

(a) Schematic showing a method for H3 and H4 level reductions via transcriptional inhibition by releasing cells into media containing raffinose. A plasmid borne construct in which the *GAL1/10* promoter drives the only pair of histone H3/H4 genes is used in the shutdown (SD) strain whereas a plasmid carrying the wild-type *HHT1-HHF1* locus is used in the control strain. (**b**) Quantified Immunoblot data shows histone H4 loss at different time-points after H3/H4 shutdown in raffinose medium from one experiment (**Supplementary Fig. 6**). (**c**) Boxplots and cumulative density graphs show volume distributions of data derived from 3D-SIM microscopy on multiple single cells (n numbers in graph) from two different cultures with tagged *MGS1* loci upon controlled histone H3/H4 shutdown. Data is presented relative to the control condition (yellow with black stripes). (**d**) MSD analysis of the *MGS1* locus in response to controlled histone level reductions. MSD graph in right panel shows enhanced chromatin movement of the *MGS1* locus after controlled histone shutdown via 60 min release into S phase in raffinose containing medium ($n^{SD(Raff)}$=30, $n^{Control(Raff)}$=34, $n^{SD(Gal)}$=52 different cells from

three independent experiments). MSD graph in left panel shows that G1 phase chromatin is more mobile than S phase chromatin but does not further increase mobility upon H3/H4 repression in raffinose containing medium ($n^{SD(Raff)}$=30, $n^{Control(Gal)}$=97 different cells from three independent experiments). All MSD graphs represent the mean ± s.e.m. of cells pooled from at least three different experiments. Boxplots in **d** represent median values, interquartile ranges and whiskers. P-values, ***P<0.001, NS=not significant, result from unequal variances t-tests. Additionally, consult **Supplementary Dataset 2** for mobility parameters and the number of cells analyzed.

Figure 6: Loss of high-mobility group protein Nhp6 links reduced nucleosome occupancy to chromatin expansion and enhanced mobility

(a) Cells carrying deletions of both NHP6A and NHP6B (*nhp6*Δ) have less nucleosomes on DNA than the wild-type cells. (**b**) Immunoblot quantification from three experiments confirms reduced histone levels in *nhp6*Δ cells and FACS analysis show similar cell cycle profiles for wild-type and *nhp6*Δ cells. (**c-d**) MSD graphs derived from high-speed live cell imaging data of *nhp6*Δ cells (shown in dark green for the *MET10* locus and in light green for the *PES4* locus) highlight enhanced chromatin mobility at two independent genomic loci *MET10* and *PES4* ($n^{MET10,\ WT}$=31, $n^{MET10,\ nhp6\Delta}$=47, $n^{PES4,\ WT}$=35, $n^{PES4,\ nhp6\Delta}$=57 different cells from three independent experiments). (**e**) Graphs show the medians and whiskers of biophysical parameters derived from imaging data and predict concurrent loss of constraining forces on chromatin. Color code as in **b**. (**f**) Boxplots of *MET10* (TetR-mCherry) foci volumes resulting from 3D-SIM microscopy in multiple asynchronous (asy.) G1 or S phase *nhp6*Δ and wild-type cells (n numbers in graph) from two different cultures indicate chromatin expansion in *nhp6*Δ cells. Color code as in **b**. Bar graphs and all MSD data (cells pooled from at least three independent experiments) represent the mean ± s.e.m.. Boxplots in **d** represent median values, interquartile ranges and whiskers. P-values, *P<0.05, **P<0.01, ***P<0.001, result from Kolmogorow-Smirnow-Tests for **e** or unequal variances t-tests for **f**. Additionally, consult **Supplementary Dataset 2** for mobility parameters and the number of cells analyzed.

Figure 7: INO80-C and checkpoint proteins regulate histone degradation and chromatin expansion in response to damage

(**a**) Representative immunoblot using H3 and H4 specific antibodies on whole cell extracts from wild-type and different mutants in response to DNA damage. Rad53 was probed to confirm checkpoint activation, tubulin or actin was used as loading control. (**b**) Bar graph shows immunoblot quantification of wild-type, checkpoint mutants and INO80-C mutants from blots derived from $n^{WT}=9$, $n^{sml1\Delta}=3$, $n^{mec1\Delta sml1\Delta}=3$, $n^{rad53\Delta sml1\Delta}=3$, $n^{arp8\Delta}=3$, $n^{ies4\Delta}=3$ different experiments. (**c**) Live single-cell microscopy of H2B-CFP in local repair, checkpoint and INO80-C mutants upon Zeocin treatment. Graphs show the mean fluorescent signals of all individual cells (cell numbers indicated in graph) per treatment over time relative to the control (Ctr.) condition. (**d**) Boxplots show TetR-mCherry focus volume distributions upon Zeocin treatment in wild-type and different mutant cells (n numbers in graph) from two different cultures in one experiment released into S phase relative to the control (Ctr.) condition. INO80-C and Mec1 are required for chromatin expansion. (**e**) Model suggesting that checkpoint signaling triggers INO80-C-dependend histone loss leading to subsequent chromatin expansion, enhanced mobility and chromatin flexibility which finally enhances repair. Uncropped blot images are shown in **Supplementary Dataset 1**. Bar graphs **b** show means ± s.e.m.. Boxplots in **d** represent median values, interquartile ranges and whiskers. P-values, *P<0.05, ***P<0.001, NS=not significant, result from unequal variances t-tests. Asterisk indicates Phosphorylation-dependent Rad53 mobility shift.

Figure 8: Reduced nucleosome occupancy enhances recombination and rescues *arp8*Δ sensitivity

(**a**) Ectopic recombination assay with two different integrative *URA3* cassettes in wild-type, *arp8*Δ and *nhp6*Δ strains. The diagram on the left highlights that recombination takes place in the context of chromatin. Bar graphs show the mean integration frequency ± s.e.m in selected mutants relative to the wild-type from three independent cultures each. (**b**) Graph showing the average recovery rate of the wild-type and different isogenic mutants from an acute treatment with different Zeocin amounts relative to the control condition (ctr.). Individual points indicate the mean over three independent replicas ± s.e.m.. (**c**) Schematic showing the workflow and the strains for H3 and H4 level reductions by means of

transcriptional inhibition as in **Fig. 5a**. (**d**) Ectopic recombination assay with two different hygromycin (hphMX4) based constructs which target either the *ATG2* or *MGS1* locus. Bar graphs show the mean integration frequency ± s.e.m of both constructs in the SD strain relative to the Ctr. strain after 120 min. pulsed histone H3/H4 reductions in Gal:Raff (galactose:raffinose, 1:20) or raffinose (Raff) medium. Three independent cultures were tested. P-values, *P<0.05, ***P<0.001, result from two-tailed paired students t-tests.

Online Methods

Yeast growth, cell cycle arrests and flow cytometry

Yeast strains and plasmids used in this study are shown in **Supplementary Table 2 and 3**. Yeast strains are all haploid and, except for the SILAC strain and the Htz1-mEos imaging control strain, derived from the W303 background (**Supplementary Table 2)**. Unless otherwise stated, yeast cultures were grown at 30 °C until logarithmic (LOG) growth-phase (OD_{600}=0.7; $1x10^7$ cells/ml) prior to Zeocin (Invitrogen) or γIR exposure at 30°C. Live cell microscopy was done at 25 °C. Flow cytometry samples were prepared as previously described[30].

For controlled *GAL1-10*::H3/H4 expression experiments coupled with gene targeting assays, GA-8386 and the relevant control strain cultures (GA-8385) were grown overnight to saturation in YP galactose/raffinose (YP Gal/Raff 1:5) medium. The next morning, cultures were inoculated in the same respective medium and grown until logarithmic (LOG) growth-phase (OD_{600}=0.7; $1x10^7$ cells/ml) prior to pulsed histone level reductions. After reaching LOG phase, cells were washed once and pulsed histone H3 and H4 level reductions were accomplished via grown in either pre-warmed 30°C YP galactose/raffinose 1:20 or YP raffinose medium for 120 minutes prior to transformation with the respective gene targeting selection cassettes. For further information about the gene targeting assay, please consult "Ectopic recombination assay" section.

For cell cycle arrest and release experiments, 1.5×10^{-8} M alpha factor (Zymo Research) was added to exponentially growing cultures at a density of OD_{600}=0.5. After 1 hour, another half of the

initial alpha factor amount was added for 30 minutes and cells were either held in G1 phase or released into pre-warmed medium for 15-25 minutes prior to Zeocin damage treatment in S phase. Cell fixation in the relevant experiments was done for 2 minutes at room temperature with 4% Paraformaldehyde.

For all Zeocin or γIR exposure experiments, saturated yeast overnight cultures were diluted to OD_{600}=0.1 the next morning and grown to LOG phase. In all assays, Zeocin was added directly to G1 arrested, S phase released or asynchronously growing LOG cultures. Cultures were incubated with the drug for 1 h prior to high-speed tracking microscopy or the indicated amount time periods for other assays and experiments (**Main Figures and Supplementary Figures**). For γIR exposure, 5ml of cell culture was transferred to a 35x10mm petri dish and irradiated in a Faxitron CellRad cell-irradiator until the indicated dose (Grey) was reached. After γIR treatment, cells were directly harvested for further downstream Western blot or mass-spectrometry-based analysis. For undamaged conditions, cells were either imaged immediately for high-speed tracking microscopy or growth was continued along with the treated samples for the indicated time periods. γIR undamaged control cells were also spread on petri dishes and harvested after irradiation of treated cells was completed. Further specific growth and treatment conditions for high-speed tracking live cell microscopy were done according to Seeber *et al.*[12].

The proteasome inhibition assay with proteasome inhibitor MG132 (Bachem) was done according to Liu *et al.*[31]. In brief, wild-type GA-6879 (**Fig. 2a**) or *erg6*Δ[32] GA-1364 (**Fig. 2b**) cells were grown to saturation overnight in SC proline (wild-type, SC medium without ammonium sulfate but 0.1% L-proline) or YPAD medium (GA-1364). The next morning, cells were inoculated to OD_{600}=0.1 in SC (wild-type) or YPAD (GA-1364) proline medium supplemented with 0.003% sodium dodecyl sulfate (SDS) and grown to OD_{600}=0.5 before addition of 75 μM MG132 or the same volume of DMSO for the control condition. After 30 min. incubation with the inhibitor, Zeocin treatment or no-damage control growth was performed for 1 hour at 30°C prior to cell harvesting for Western blot analysis.

For H2B-CFP (Strain GA-3364 and derivatives) and 2-foci (Strain GA-9777) live cell fluorescent microscopy, LOG phase cells were trapped with 3 pulses of 5 psi pressure in CellASIC plates of the ONIX microfluidic perfusion system (Merck Millipore). All perfusions were done at a continuous flow rate of 2 psi pressure. After a 20-30 minute recovery phase, cells were treated for 30 minutes with the indicated amount of Zeocin prior to high-speed CFP-RFP tracking microscopy. The recovery phase

584 of H2B-CFP tagged cells was 20 minutes after which they were treated with a pulse of Zeocin for 1 hour
585 and H2B-CFP fluorescence was followed for additional 40 minutes after treatment.

586 For constitutive H3/H4 expression or reduction experiments, GA-8386 and the relevant control
587 strain cultures (GA-8385) were grown overnight to saturation in YP Galactose (YP Gal) or YP
588 galactose/raffinose (YP Gal/Raff) medium and inoculated in the same respective media prior to Zeocin
589 treatment and cell harvest. For controlled H3/H4 shutdown experiments, overnight growth and growth
590 to OD600=0.5 was done with the same strains in YP Gal/Raff (Gal/Raff 1:5 ratio) medium which confers
591 wild-type H3/H4 expression levels. After G1 phase arrest at 25°C with alpha factor in YP Gal/Raff
592 medium, cells were released either into pre-warmed 25°C YP Gal or YP Raff medium for 60 minutes
593 prior to fixation for structural illumination microscopy (SIM) or live cell high-speed imaging.

594 In all other Western blot and label-free mass spectrometry experiments, cells were grown in full
595 medium (YPD) and cell growth for microscopy experiments was either done in synthetic complete (SC)
596 medium or sterile filtered, non-autoclaved YPD medium.

597 **Genome-wide nucleosome mapping**

598 Strains tested for changes in nucleosome occupancy (GA-6879 and GA-8386) were grown in
599 appropriate media to OD_{600}=0.8. Cultures were split into two and one of them was treated with Zeocin
600 (500µg/ml) for 1 hour. At this point the OD_{600} absorbance of each sample was measured and *Candida*
601 *glabrata* cells were spiked in to 1/10 according to the sample OD_{600}. Cells were washed three times with
602 ice cold TBS (20mM Tris-HCl pH 8.0 and 150mM NaCl) and lysed by beat beating in micrococcal
603 nuclease (MNase) digestion buffer (10 mM Tris pH 8.0, 50 mM NaCl, 5mM MgCl2, 1 mM CaCl2,
604 1mM beta-mercaptoethanol, 0.5 mM spermidine, 0.075% NP40). The obtained chromatin samples were
605 MNase digested to isolate mono-nucleosomes and sequencing libraries were prepared according to the
606 method described in Wiechens *et al.*[33]. Paired end libraries of MNase digested chromatin were
607 sequenced using illumina HiSeq technology. Fastq files containing raw reads were aligned to the *S.*
608 *cerevisiae* and *C. glabrata* reference genomes by Bowtie2 with option of maximum fragment length
609 500 for nucleosome fragments. The nucleosome dyads at each position were calculated in a defined
610 window flanking the transcription start site (TSS). The sum of dyads at a given position across all TSS

was then normalized by the total number of nucleosome dyads across all position flanking ~ 6000 TSSs in the given window. The reads were further normalized by dividing the fraction of *C. glabrata* reads in the sample. For low and high expression gene plots, the TSS of 15% highly and 15% lowly expressed genes were chosen. The data was smoothed using a 50 bp sliding window for graphical representation. Plots were generated with python's plotting modules matplotlib and pylab.

Quantitative Western Blot Analysis

The total protein content in the relevant samples was determined with the Quant-iT protein assay kit (ThermoFisher Scientific) and 8.75 µg of total protein was loaded and run on Criterion TGX Stain-Free 8-16% (Biorad) gels under SDS denaturing electrophoresis conditions. Rapid fluorescent detection of all proteins in the gel or on the membrane was done according to the manufacturer's specifications and protein transfer on PVDF membranes was performed using the Trans-Blot Turbo system. All antibodies used for subsequent immunodetections are listed in **Supplementary Table 4**. Rad53 protein was detected using a custom-made mouse monoclonal antibody (GenScript) against FHA2 domain of Rad53. Anti-γH2A was similarly a custom-made polyclonal antibody, that is specific for phospho-S129 in yeast H2A. Titration curves of histone H3 and histone H4 antibodies done to work within the linear detection range prior to use (**data not shown**).

Chromatin Fractionation and Quantitative Mass Spectrometry

For SILAC based mass spectrometry, lysine and arginine double labeling of the *lys2Δ arg4Δ* strain yAG-06A was achieved by growth for at least ten generations in "heavy" medium as described previously in Gruhler *et al.*[34]. After growth to LOG phase or at G1 cell cycle arrest, "light" labeled cells (or "heavy" labeled cells for label-swap controls) were treated for 1h with Zeocin and mixed 1:1 based on exact cell count with "heavy" labeled ("light" for label-swap control), non-treated control cells. Prior to mixing, FACS and Western blot samples were taken to test for cell cycle distribution and DDC activation.

Chromatin fractionation was performed as previously described[35] with the modification that chromatin obtained from SILAC labeled yeast samples was resuspended in urea buffer (50 mM Tris-HCl pH 7.5, 6 M Urea, 1% SDS, 5 mM EDTA) sonicated for optimal solubilizing of proteins followed by a TCA protein precipitation step prior to downstream mass spectrometric analysis. To avoid

carbamylation in urea buffer, samples were kept below 20°C and quickly processed. Control samples from whole cell extract (WCE), supernatant (SUP) and chromatin fraction (CHR) were analyzed with SDS-PAGE (Novex 8–16% Tris-Glycine Gel, Invitrogen) gel electrophoresis followed by Coomassie staining.

Samples for label-free histone quantification came from LOG phase or G1 phase arrested cells grown in YPD medium. After γIR treatment, 5 ml of culture were fixed with 10% TCA on ice. Whole cell lysates were obtained with bead-beating cells at 4°C in urea buffer (50 mM TRIS pH 7.5, 6 M Urea, 1% SDS, 5 mM EDTA). 100-150 µg total protein was precipitated for downstream MS analysis.

For both SILAC and label-free samples, reduction and alkylation of cysteines was performed in 20 µl RCM buffer by adding 4 µl 100 mM TCEP for 30 min followed by 4 µl 250mM iodoaeetamide for another 30 min (in the dark), both at room temperature. Prior to the addition of 20 µl of 1 mg/ ml LysC (Wako, Japan) the extracts were twofold diluted to keep a final HEPES concentration of 20 mM. The first digest was performed overnight at 25°C. After 2-fold dilution, 100 µl of 0.5 mg/ ml trypsin was added and the second digest was performed at 37°C overnight. Samples were desalted using SepPak C18 columns (Waters) and eluates were dried to completion in a SpeedVac (ThermoFisher Scientific).

Both SILAC and label-free LC/MS/MS analyses was performed on an Easy-nLC 1000 pump coupled to an LTQ Orbitrap Velos mass spectrometer (ThermoFisher Scientific) using a Digital PicoView ion source (New Objective). Peptides were separated on a New Objective analytical column (75 µm x 25 cm, Reprosil, 3 µm) with a 150 min. 0.1% formic acid/acetonitrile gradient. The flow rate was 200 nL/min and injection volumes were adapted accordingly for 1 µg peptides on column.
Data were acquired in a Top20 data dependent analysis mode. MS scans were acquired at a resolution of 60000 over a range of *m/z* 350 to 1200. Label-free peptides were identified searching SwissProt using Mascot 2.4 (Matrix Science) and compiled in Scaffold 3.0 (Proteome Software). SILAC peptides were identified with MaxQuant 1.4.1.2. searching the SGD database. Two missed cleavage sites were allowed.

Label-free relative quantification of histones was done by generating the extracted ion chromatogram for the peptide precursor mass, integrating the peak areas (using QuanBrowser,

665 ThermoFisher Scientific) which are then used for calculating the peptide ratios. The average of those
666 ratios determines the ratio of the histones (reference untreated or wild type sample). This method is more
667 precise than the TOP 3 TIC method used in Scaffold. Untreated or wild type references were set to 1.
668 We used 2 peptides from each ALF, KPK1, IF4A and IFSA1 protein as internal references for the
669 quantification of relative histone abundances in each run. Histone level ratios in SILAC samples are
670 shown as the average from all non-label-swap or label-swap replicas. Ratios were derived from the
671 MaxQuant peptide list taking into account only core histone peptides reported as not being subject to
672 post translational modifications[21]. Significance was addressed by blotting the distribution of all protein
673 ratios from the MaxQuant protein-groups list together with the protein intensities. Core histones were
674 always the most abundant proteins measured and reside within the first significant interval. The
675 MaxQuant protein-groups list was filtered by removing all contaminants, all reverse hits and proteins
676 quantified with less than 2 peptides. The cutoff for variability was set to 30%. Normalization was done
677 manually taking the 35 most abundant proteins (histones excluded). The MaxQuant peptide list (except
678 for the G1 experiment) was filtered accordingly without variability cutoff and only taking peptides into
679 account that had a L/H or H/L count greater than 3. Normalization was done manually taking the top
680 10% most abundant peptides (histone peptides excluded).

681 **Live cell microscopy and Image Analysis**

682 Live microscopy was done on a temperature controllable Olympus IX81 microscope with a Yokogawa
683 CSU-X1 scanning head equipped with two EM-CCD EvolveDelta (Photometrics) cameras, an ASI MS-
684 2000 Z-piezo stage and a PlanApo x100, NA 1.45 total internal reflection fluorescence microscope oil
685 objective and Visiview software. For mRFP-GFP or mRFP-CFP high-speed tracking, fluorophores were
686 excited with lasers at 561 nm (mCherry or mRFP) and 491 nm (GFP) or 440 nm (CFP) and emitted
687 fluorescence was acquired simultaneously on separate cameras (Semrock FF01-617/73-25 filter for
688 mCherry/mRFP and Semrock FF02-525/40-25 filter for GFP or Semrock FF01-475/42-25 for CFP).
689 High-speed time-lapse series were conducted taking 8 optical slices per stack either every 80 ms for 1
690 min or 300 ms for 2 min, with 10 ms exposure times per slice respectively. Time-lapse image stacks
691 were analyzed as in Dion *et al.*[9], using a custom made ImageJ (FIJI) plug-in[36] to extract coordinates of
692 locus position from the movies. Phototoxicity was tested by exposing wild-type cells (GA-6879) to

standard imaging conditions and following outgrowth for 5 h by morphological analysis, comparing them with unexposed cells. Time-series acquired from Strains GA-9227 and GA-9777 (Two-spot data) were deconvolved using Huygens Remote Manager, channel-aligned and cropped to contain one single cell/nucleus with the two respective fluorescent spots. Spot tracking over time was done with the ImageJ plugin TrackMate included in Fiji[37]. Boxplot graphs were generated by plotting all measured distances of treated or untreated cells. Relative MSD analysis was performed with KNIME[38] using the workflow provided in the supplementary information (**Supplementary Dataset 2**). For each frame, the distance vector of tracks in two channels was measured by selecting the two spots with minimal distance. We performed an MSD analysis on the distance vectors for all frames and tracks with a maximum MSD(t) value bigger than 10 μm² were considered as outliers (due to mis-matching two distant tracks) and removed from the analysis. Relative MSD vs. t was averaged over all tracks and plotted using R.

For H2B-CFP (GA-3364 and derivatives) live cell microscopy, cells trapped in CellASIC plates were mounted on the same microscopic setup and different stage positions of the whole field of view were excited with a 440nm laser and the emitted fluorescence was acquired on a EM-CCD EvolveDelta (Photometrics) camera using a Semrock FF01-475/42-25 emission filter. The Htz1-mEos (GA-9594) and Nup49-GFP (GA-5816) control strain was excited at 491 nm and fluorescence was recorded through a Semrock FF02-525/40-25 filter. Time-lapse series (120 min total) of 100 optical slices per stack (200nm intervals) were acquired for 12 time points at 10 min intervals, with each slice being exposed for 10 msec per laser line. Bright-field images were acquired using a CoolLED diode. Images were deconvolved using the Huygens Remote Manager software. For image analysis, deconvolved maximum intensity projections were analyzed as a merged stack in ICY. Nuclei were detected and segmented using HK means and active contours and followed through the time series. The integrated nuclear intensity was calculated for each cell nucleus and the average intensity of all single cells per condition was plotted over time. The t0 time-point to 100% intensity (via average of the first two timepoints) and the Zeocin treatment condition of each strain is shown relative to its control.

Structured Illumination Microscopy and Image Analysis

Structured illumination images were acquired on a Zeiss Elyra S.1 microscope with a Andor iXon 885 EMCCD camera using a HR diode 488 100nW solid state laser, BP 525-580 + LP 750 filter and a PLAN-

APOCHROMAT 63x N.A. 1.4 oil DIC objective lens. Cells were first fixed in PFA 4%, washed 3 times in PBS and then attached to a thin SIM grade Zeiss 1.5 glass coverslip using Concanavalin A. Cells were fully sectioned by 50-65 slices with 0.1 nm intervals taken at 60 ms exposures per slice using 5 rotations of the illumination grid. Brightfield images of the cells were also acquired using an X-Cite PC 120 EXFO Metal Halide lamp. Zen Black was used to process the images using automatic settings with the Raw Scale option selected. 3D stacks were then analyzed by using pixel classification and a custom Matlab script to determine the spot volumes and other features as follows. We used a fully automated nucleus and spot segmentation workflow that allowed the individual detection and feature extraction where a manual or even a semi-automated delineation would be unfeasible. The image processing software was realized within the MATLAB environment and supported by the supervised learning-based pixel classification toolkit Ilastik[39]. The voxels corresponding to the nucleus, the inner spot and background regions are annotated interactively by brush strokes during the training phase. Features calculated at the labeled pixels and their local neighborhood are then used to train a pixel classifier based on a Random Forest ensemble learning method. The processing software provides an automated whole segmentation of all the nuclei and spots present in the scene. The image processing function is later used in a parallelized batch process on multiple processors. After detection and segmentation of nuclei and spots, the program produces a graphical output in form a maximum intensity projection with delineation of the nucleus, the spots and the unique ID integer that identifies the nucleus candidate. In addition, 3D logical masks corresponding to the classes “spot” and “nucleus” are computed. Finally, the program generates an ascii file where the key features like volume and solidity 3D and descriptive statistics are listed for all detected nuclei and foci. The solidity factor is calculated as the proportion of pixels in the 3D convex hull. For statistical analysis and data representation, raw volumes were filtered to exclude spots smaller than 200 and greater than 4000 voxels, the control (Ctr.) condition was set to 1 and Zeocin treated spot or nuclei volume distributions are shown relative to the untreated control. The distributions were plotted with R as boxplot graphs or a cumulative density functions.

Microscopy and Image Analysis of Fixed Samples

Microscopy of fixed GA-9777 samples was done with the same Olympus IX81 microscope setup mentioned before. Cells were fixed with paraformaldehyde and attached to a thin SIM grade Zeiss 1.5

glass coverslip using Concanavalin. We acquired 70 optical slices in 100nm intervals with the 561 nm and 491 laser line (130 ms exposure each). Bright-field images were acquired using a CoolLED diode. Images were deconvolved using Huygens Remote Manager, channel-aligned and 3D inter-spot distances (Δd) between the GFP and mRFP centroids were measured with the Imaris software. The distribution of all measured distances per condition was plotted with R as a boxplot graph or a cumulative density function.

Ectopic Recombination Assays

For **Fig. 8a**: As used in wild-type cells, *arp8*Δ cells and cells depleted for *NHP6A*/*NHP6B*

For specific growth conditions, please consult the "*Yeast growth, cell cycle arrests and flow cytometry*" section. Equal amounts of exponentially growing wild-type (GA-6879) *arp8*Δ (GA-8132) and *nhp6*Δ (GA-9771) were transformed with the transformation protocol either with a linearized *URA3* plasmid (pRS406 cut with *Stu*I) presenting 800 bp homology to the W303 *ura3-1* locus or a *mgs1::caURA3* PCR fragment (template plasmid #1050) presenting 40 bp and 42 bp upstream and downstream homology to the *MGS1* locus. As a control, the centromeric circular plasmid #2422 (ADE2, hphMX4, Cen/ARS), which is maintained in yeast cells ectopically, was transformed alongside with the URA3 integration cassettes. Primers were #7297:

(GTTTTTTTACGCTTGAGGCGCATTGCATTGCTGGCACGTTTTTGTGCGGATCC CCGGGTTAATTAA) and #7298:

(CGTATATGTTCTAATATATCTCAGATGGGCCCGCGAGACTTTGCGCGTTGGCCGATTCATTA).

After transformation, cells were split and plated on SC-URA plates (100 µl) to select for transformants resulting from integration and on and YPD + Hygromycin B plates to select for cells containing the plasmid. The numbers of Ura+ and Leu+ transformants obtained from each reaction were compared to calculate the relative integration rate for each strain, with that of a wild-type strain arbitrarily set to 1 as a reference. Growth was scored in biological quadruplicates and each transformation was done with four technical replicates.; results were averaged.

For **Fig. 8c-d**: "Ctr." cells and Gal:H3/H4 "histone shutdown" cells

For specific growth conditions, please consult the "*Yeast growth, cell cycle arrests and flow cytometry*" section. After pre-growth in YP Galactose/Raffinose 1:5 medium, equal amounts of exponentially growing control (GA-8385) and Gal:H3/H4 "histone shutdown" (GA-8386) cells were pulse-reduced for histone H3 and H4 levels via 2 hour growth in either YP Galactose/Raffinose 1:20 or YP Raffinose medium. After the histone-reduction pulse, transformations were done with either an *atg2::hphMX4* PCR fragment (PCR product – *ATG2::hygro*, template plasmid #1049) presenting 40 bp and 40 bp upstream and downstream homology to the *ATG2* locus or a *mgs1::hphMX4* PCR fragment (PCR product – *MGS1::hygro*, template plasmid #1049) presenting 40 bp and 42 bp upstream and downstream homology to the *MGS1* locus. As a control, the centromeric circular plasmid #282 (LEU2, Cen/ARS), which is maintained in yeast cells ectopically, was transformed alongside with the hphMX4 PCR integration cassettes.

Primers for PCR product – *ATG2::hygro* were #6302:

(ATAGCCTTGGCGAGTTTTCCGTACATTGAAGAATTCGCCAAGCGGATGCCGGGAGCAGAC)

and #6303:

(GGGATTTTTGGCTCAAGGTGTGGTGGCCCCTTTTCTAAGGGTGAGCTGATACCGCTCGCC)

Primers for PCR product – *MGS1::hygro* were #7297:

(GTTTTTTTACGCTTGAGGCGCATTGCATTGCTGGCACGTTTTTGTGCGGATCCCCGGGTTAATTAA)

and #7298:

(CGTATATGTTCTAATATATCTCAGATGGGCCCGCGAGACTTTGCGCGTTGGCCGATTCATTA).

After transformation, cells were split and plated on YPGal +Hygromycin B plates (100 µl plated) to select for transformants resulting from integration of *ATG2::hygro* or *MGS1::hygro* and on and SCGal -LEU plates (10 µl plated) to select for cells containing the plasmid. The numbers of hphMX4+ and LEU+ transformants obtained from each reaction were compared to calculate the relative integration

rate for each strain, with that of a wild-type strain arbitrarily set to 1 as a reference. Growth was done in biological quadruplicates and each transformation was done with four technical replicates; results were averaged.

Recovery assay

Equal amounts of exponentially growing (YPAD medium, cell density approx. $1x10^7$ cells/ml) WT (GA-6879), *arp8*Δ (GA-8132), *nhp6*Δ (GA-9771) and *arp8*Δ*nhp6*Δ cells (GA-9815) were treated in triplicates with increasing amounts of Zeocin (100, 250 and 500 µg/ml). After 1 hour of treatment, cells were washed once with fresh, pre-warmed (30°C) YPAD medium and grown for an additional hour in YPAD without Zeocin. After this step, the cell density was accurately determined in three technical replicates and used as a later correction factor for cell growth within the 1 hour of Zeocin treatment and the 1 hour growth in YPAD of the control (Ctr.) versus the Zeocin treated cultures (Zeo^{100} – Zeo^{500}). Aliquots were removed and plated in a dilution row. Growing colonies vs. plated cells were quantified, the Ctr. situation served as reference point and was set to 100%.

Rad52-YFP Recovery Assay

Cells grown to saturation overnight in sterile filtered, non-autoclaved YPD medium were diluted the next morning and the experiment was started when reaching OD_{600}=0.6. Wild type (GA-9772) and *nhp6*Δ cells (GA-9771) were treated with 250 µg/ml Zeocin for 30 minutes. Zeocin was washed away and Rad52-YFP foci formation was followed over a total time-course of 16 hours taking microscopic images at the following time points: 0 min, 20 min, 40 min, 1h, 2h, 4h, 6h, 8h, 10h, 12h, 14h and 16h. Rad52-YFP foci were imaged with the same microscopic setup as mentioned above acquiring 50 optical slices in 200 nm intervals with 50 ms exposure time using a 514 nm laser with appropriate emission filters. Images were deconvolved as described above, maximum intensity projected and the binary (+ or -) content of Rad52-YFP foci all living cells at each time point in each strain was counted. The average amount of Rad52-YFP foci containing cells per time point was plotted and is shown together with a logarithmic fit.

Estimating the anomalous diffusion exponent α and the diffusion coefficient

Please refer to Supplementary Notes.

Estimating the effective spring coefficient k_c

Please refer to Supplementary Notes.

Statistics and Reproducibility

All chromatin mobility data (spot tracking) are pooled from three independent experiments (**Fig. 3a, Fig. 5d, Fig. 6cd, Supplementary Fig. 5a**). Statistical analysis testing the significance of the biophysical parameters derived from the imaging data was performed with Matlab using the Kolmogorow-Smirnow-Test (**Fig. 3b, Fig. 5d, Fig. 6e, Supplementary Fig. 5b, Supplementary Fig. 7cd**). All SIM microscopy data from individual single cells are pooled and were derived from one experiment. The data was analysed with RStudio using unequal variance t-tests (**Fig. 3d, Fig. 5c, Fig. 6f, Fig. 7d**). For H2B-CFP single cell fluorescent microscopy analysis, the integrated nuclear intensity was calculated for each cell nucleus and the average intensity of all single cells per condition was plotted over time. All data from single cells originating from three independent cultures on three different days (**Fig. 1d H2B-CFP**); two independent cultures on two different days (**Fig. 1d** Htz1-mEos, **Fig. 7c** *rad51*Δ*/sml1*Δ*/arp8*Δ); two independent cultures from the same day (**Fig. 7c** *rad53*Δ*sml1*Δ). Recombination efficiency and cell recovery experiments were performed in triplicates (three independent cell cultures) and Excel was used to perform two-tailed student's t-tests (**Fig. 8 abd**). Chromatin fractionations were repeated with three independent cultures (**Supplementary Fig. 1fg**) or two independent cultures (**Fig. 1a, Supplementary Fig. 1h, Supplementary Fig. 3ij**). Nucleosome mapping data for the wild-type strain (GA-6879) was performed on four independent cultures (**Fig. 1c, Supplementary Fig. 2e**); for the H3/H4 transcription independent strain (GA-8386) the experiment was done once (**Supplementary Fig. 4b**) but new data deriving from four independent cultures shows the same effect (**data not shown**). The kinetics of the Rad52-YFP recovery assay on wild-type and *nhp6*Δ cells (12 different time-points) was performed once but done on the single cell level.

Data availability statement

The EBI project ID for the nucleosome-Seq data in this study is PRJEB14701. Source data for Figs. 1bd, 2abc, 5b, 7bc, 8a, Supplementary Fig. 2g and mass spectrometry data (Supplementary Dataset 4-9) are available with the paper online. Other data supporting the findings of this study are available from

the corresponding authors upon request.

References (Online Methods only)

30. Haase, S.B. & Lew, D.J. Flow cytometric analysis of DNA content in budding yeast. *Methods Enzymol* **283**, 322-32 (1997).

31. Liu, C., Apodaca, J., Davis, L.E. & Rao, H. Proteasome inhibition in wild-type yeast Saccharomyces cerevisiae cells. *Biotechniques* **42**, 158, 160, 162 (2007).

32. Lee, D.H. & Goldberg, A.L. Selective inhibitors of the proteasome-dependent and vacuolar pathways of protein degradation in Saccharomyces cerevisiae. *J Biol Chem* **271**, 27280-4 (1996).

33. Wiechens, N. et al. The Chromatin Remodelling Enzymes SNF2H and SNF2L Position Nucleosomes adjacent to CTCF and Other Transcription Factors. *PLoS Genet* **12**, e1005940 (2016).

34. Gruhler, A. et al. Quantitative phosphoproteomics applied to the yeast pheromone signaling pathway. *Mol Cell Proteomics* **4**, 310-27 (2005).

35. Pasero, P., Duncker, B.P., Schwob, E. & Gasser, S.M. A role for the Cdc7 kinase regulatory subunit Dbf4p in the formation of initiation-competent origins of replication. *Genes & Development* **13**, 2159-2176 (1999).

36. Sage, D., Neumann, F.R., Hediger, F., Gasser, S.M. & Unser, M. Automatic tracking of individual fluorescence particles: application to the study of chromosome dynamics. *IEEE Trans Image Process* **14**, 1372-83 (2005).

37. Schindelin, J. et al. Fiji: an open-source platform for biological-image analysis. *Nat Methods* **9**, 676-82 (2012).

38. Dietz, C. & Berthold, M.R. KNIME for Open-Source Bioimage Analysis: A Tutorial. *Adv Anat Embryol Cell Biol* **219**, 179-97 (2016).

39. Sommer, C. & Gerlich, D.W. Machine learning in cell biology - teaching computers to recognize phenotypes. *J Cell Sci* **126**, 5529-39 (2013).

Figure 1

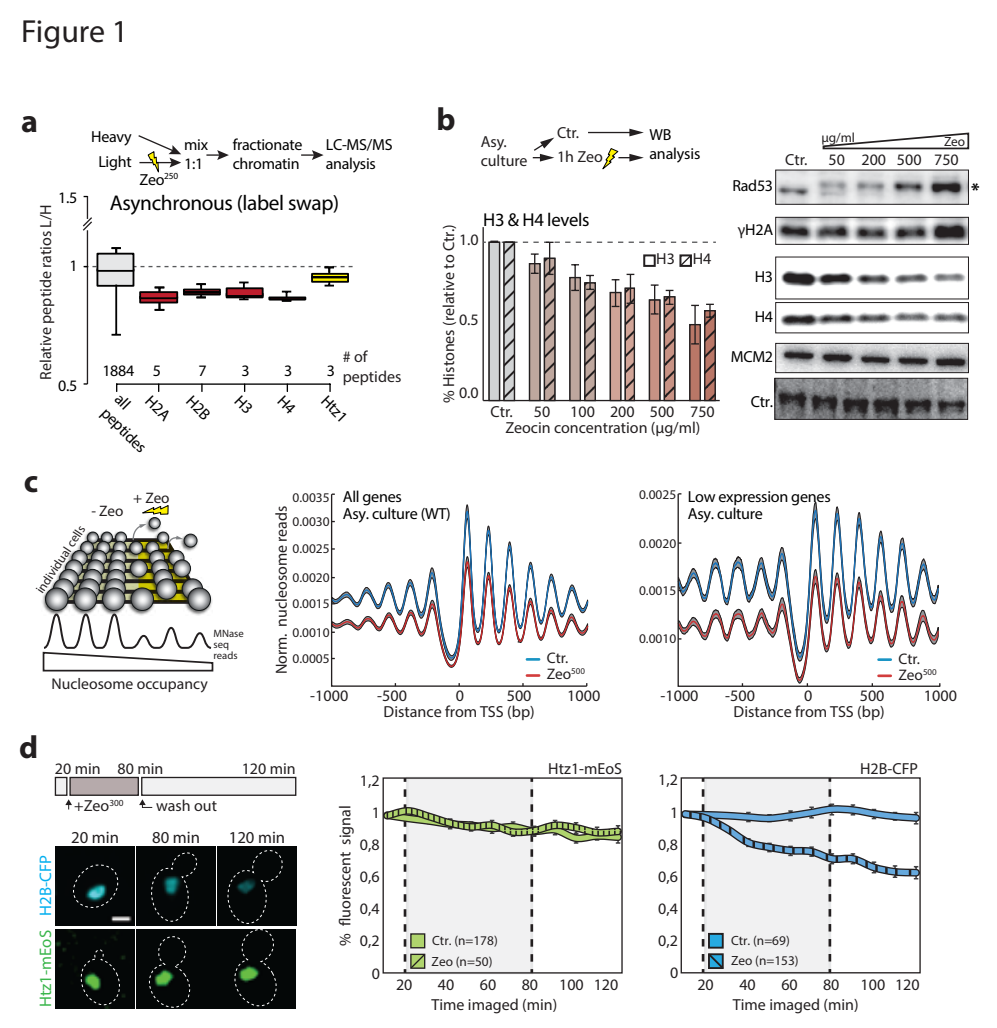
a
Heavy
Light
Zeo250
mix
1:1
fractionate
chromatin
LC-MS/MS
analysis
Asynchronous (label swap)
Relative peptide ratios L/H
1.5
1
0.5
1884
5
7
3
3
3
# of peptides
all peptides
H2A
H2B
H3
H4
Htz1
b
Asy. culture
Ctr.
1h Zeo
WB analysis
H3 & H4 levels
% Histones (relative to Ctr.)
1.0
0.5
0.0
H3
H4
Ctr.
50
100
200
500
750
Zeocin concentration (µg/ml)
µg/ml
Zeo
Ctr.
50
200
500
750
Rad53
*
γH2A
H3
H4
MCM2
Ctr.
c
- Zeo
+ Zeo
individual cells
MNase seq reads
Nucleosome occupancy
All genes
Asy. culture (WT)
Norm. nucleosome reads
0.0035
0.0030
0.0025
0.0020
0.0015
0.0010
0.0005
Ctr.
Zeo500
-1000
-500
0
500
1000
Distance from TSS (bp)
Low expression genes
Asy. culture
0.0025
0.0020
0.0015
0.0010
Ctr.
Zeo500
-1000
-500
0
500
1000
Distance from TSS (bp)
d
20 min
80 min
120 min
+Zeo300
wash out
20 min
80 min
120 min
H2B-CFP
Htz1-mEoS
Htz1-mEoS
% fluorescent signal
1,2
1
0,8
0,6
0,4
0,2
0
Ctr. (n=178)
Zeo (n=50)
20
40
60
80
100
120
Time imaged (min)
H2B-CFP
1,2
1
0,8
0,6
0,4
0,2
0
Ctr. (n=69)
Zeo (n=153)
20
40
60
80
100
120
Time imaged (min)

Figure 2

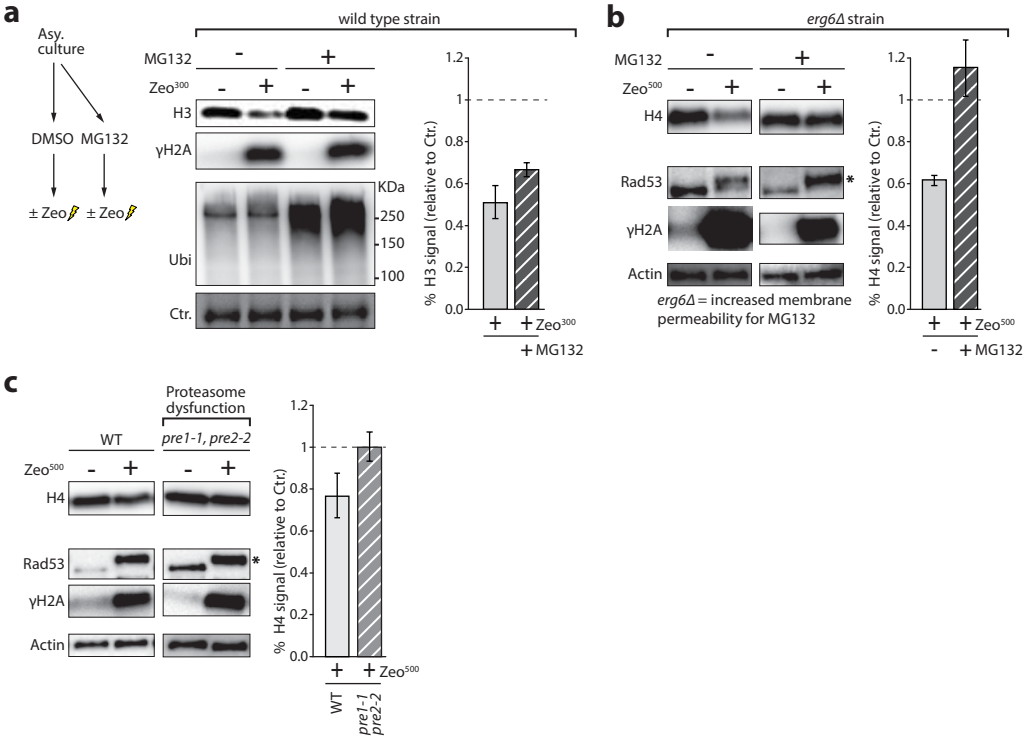
a
Asy. culture
DMSO
MG132
± Zeo
± Zeo
wild type strain
MG132
Zeo300
H3
γH2A
Ubi
Ctr.
KDa
250
150
100
% H3 signal (relative to Ctr.)
+ Zeo300
+ MG132
b
erg6Δ strain
MG132
Zeo500
H4
Rad53
γH2A
Actin
erg6Δ = increased membrane permeability for MG132
% H4 signal (relative to Ctr.)
+ Zeo500
+ MG132
c
Proteasome dysfunction
WT
pre1-1, pre2-2
Zeo500
H4
Rad53
γH2A
Actin
% H4 signal (relative to Ctr.)
+ Zeo500
WT
pre1-1 pre2-2

Figure 3

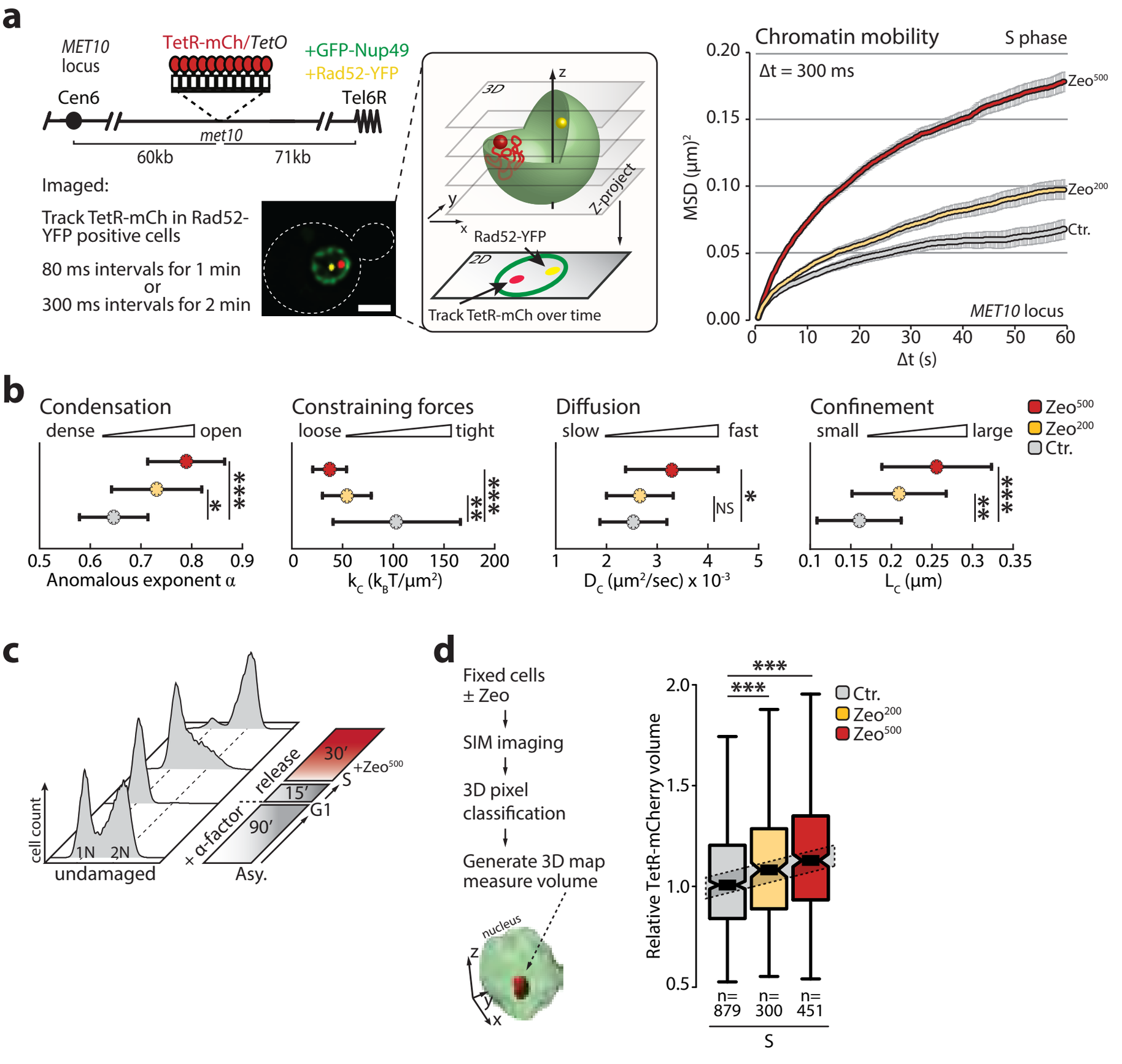
a
MET10 locus
TetR-mCh/TetO
+GFP-Nup49
+Rad52-YFP
Cen6
Tel6R
met10
60kb
71kb
Imaged:
Track TetR-mCh in Rad52-YFP positive cells
80 ms intervals for 1 min
or
300 ms intervals for 2 min
3D
z
y
x
Z-project
Rad52-YFP
2D
Track TetR-mCh over time
Chromatin mobility
S phase
Δt = 300 ms
Zeo500
Zeo200
Ctr.
MET10 locus
MSD (μm)2
Δt (s)
b
Condensation
dense
open
Anomalous exponent α
Constraining forces
loose
tight
kC (kBT/μm2)
Diffusion
slow
fast
NS
DC (μm2/sec) x 10-3
Confinement
small
large
LC (μm)
Zeo500
Zeo200
Ctr.
c
cell count
1N
2N
undamaged
+ α-factor
release
30′
15′
90′
+Zeo500
S
G1
Asy.
d
Fixed cells
± Zeo
SIM imaging
3D pixel classification
Generate 3D map measure volume
nucleus
Relative TetR-mCherry volume
Ctr.
Zeo200
Zeo500
n= 879
n= 300
n= 451
S

Figure 4

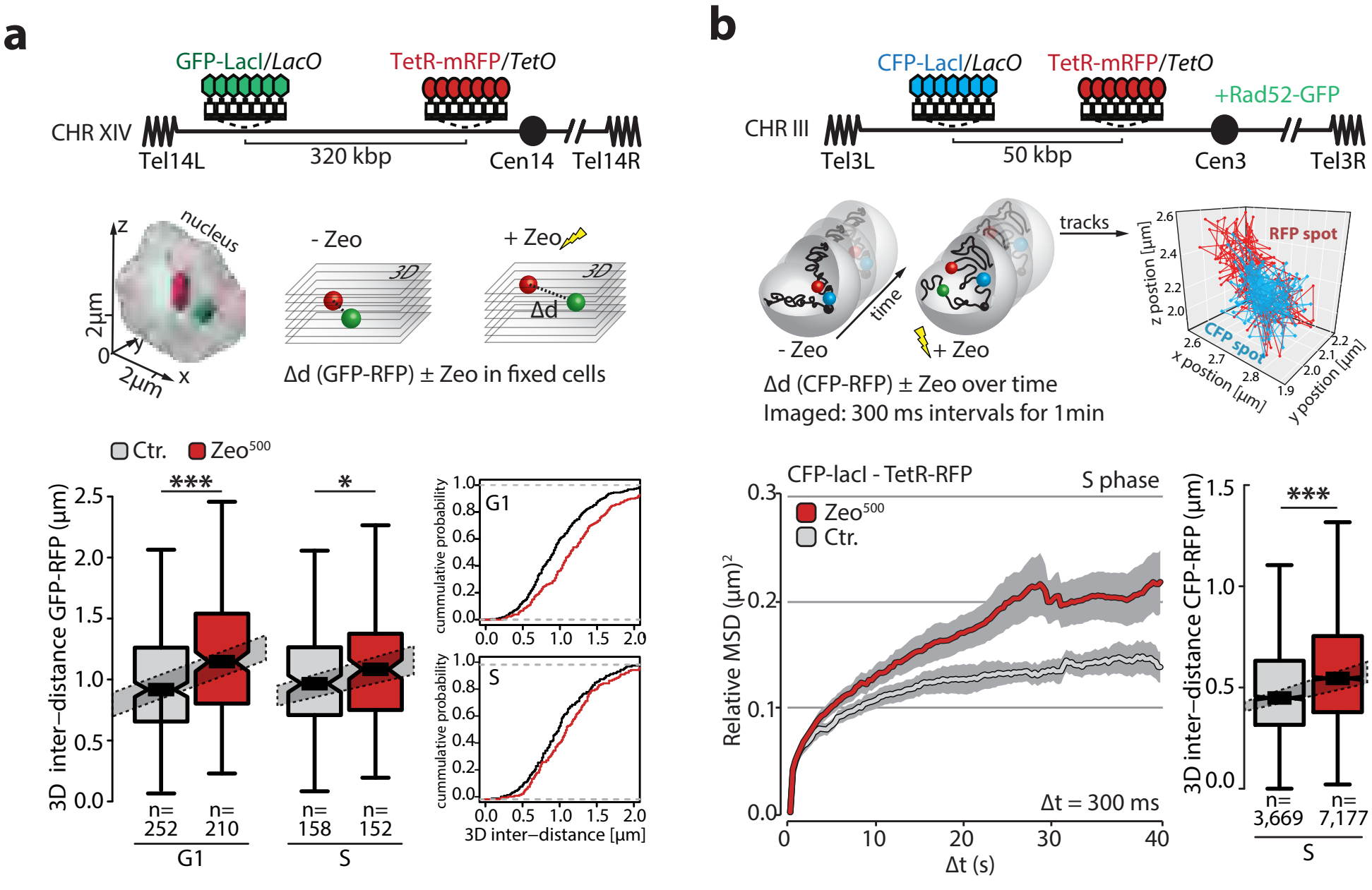
a
GFP-LacI/LacO
TetR-mRFP/TetO
CHR XIV
Tel14L
320 kbp
Cen14
Tel14R
nucleus
z
2µm
y
0
2µm
x
- Zeo
+ Zeo
3D
Δd
Δd (GFP-RFP) ± Zeo in fixed cells
Ctr.
Zeo500
***
*
3D inter−distance GFP-RFP (µm)
n= 252
n= 210
n= 158
n= 152
G1
S
cummulative probability
3D inter−distance [µm]
b
CFP-LacI/LacO
TetR-mRFP/TetO
+Rad52-GFP
CHR III
Tel3L
50 kbp
Cen3
Tel3R
time
- Zeo
+ Zeo
tracks
RFP spot
CFP spot
z postion [µm]
x postion [µm]
y postion [µm]
Δd (CFP-RFP) ± Zeo over time
Imaged: 300 ms intervals for 1min
CFP-lacI - TetR-RFP
S phase
Zeo500
Ctr.
Relative MSD (µm)²
Δt = 300 ms
Δt (s)
3D inter−distance CFP-RFP (µm)
n= 3,669
n= 7,177
S

Figure 5

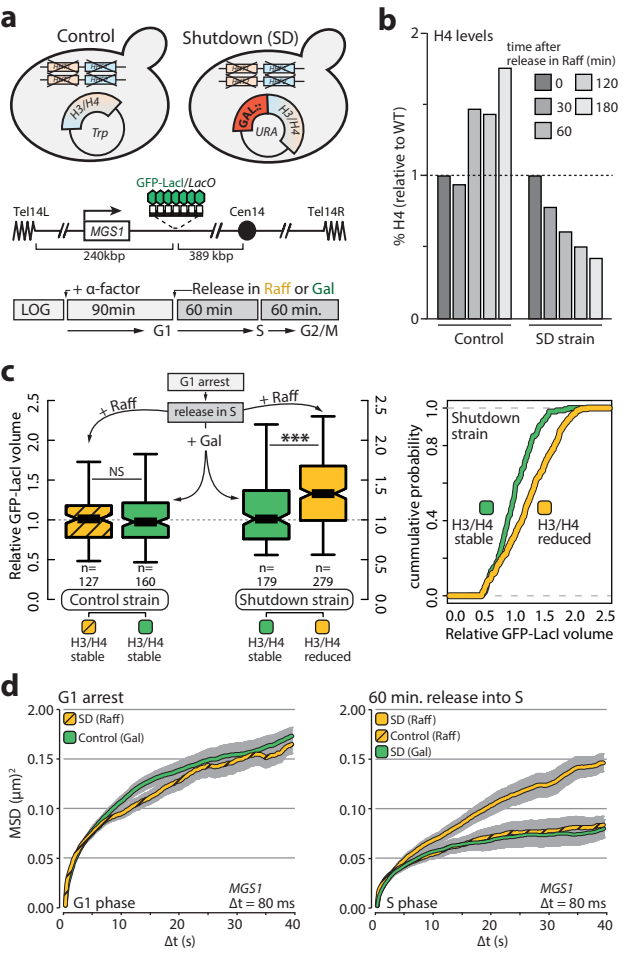
a
Control
Shutdown (SD)
HB/H4
Trp
GAL1
H3/H4
URA
GFP-LacI/LacO
Tel14L
MGS1
Cen14
Tel14R
240kbp
389 kbp
+ α-factor
Release in Raff or Gal
LOG
90min
60 min
60 min.
G1
S
G2/M
b
H4 levels
time after release in Raff (min)
0
30
60
120
180
% H4 (relative to WT)
Control
SD strain
c
G1 arrest
release in S
+ Raff
+ Raff
+ Gal
NS
***
Relative GFP-LacI volume
n= 127
n= 160
n= 179
n= 279
Control strain
Shutdown strain
H3/H4 stable
H3/H4 stable
H3/H4 stable
H3/H4 reduced
Shutdown strain
H3/H4 stable
H3/H4 reduced
cummulative probability
Relative GFP-LacI volume
d
G1 arrest
SD (Raff)
Control (Gal)
MSD (μm)²
G1 phase
MGS1
Δt = 80 ms
Δt (s)
60 min. release into S
SD (Raff)
Control (Raff)
SD (Gal)
S phase
MGS1
Δt = 80 ms
Δt (s)

Figure 6

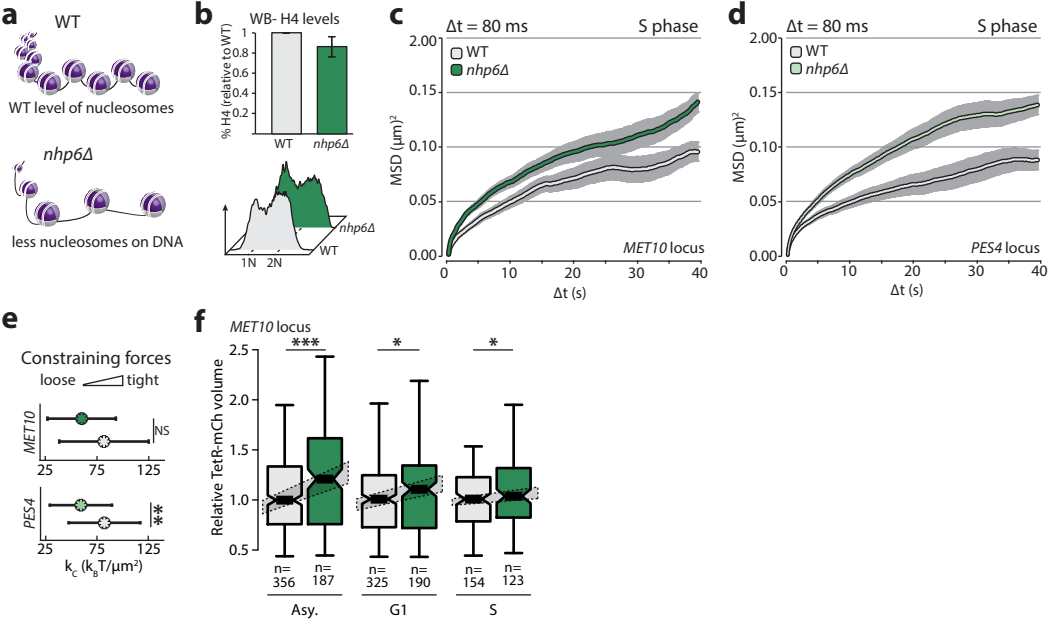
a
WT
WT level of nucleosomes
nhp6Δ
less nucleosomes on DNA
b
WB- H4 levels
% H4 (relative to WT)
1
0.8
0.6
0.4
0.2
WT
nhp6Δ
nhp6Δ
WT
1N
2N
c
Δt = 80 ms
S phase
WT
nhp6Δ
MSD (μm)²
2.00
0.15
0.10
0.05
0.00
0
10
20
30
40
Δt (s)
MET10 locus
d
Δt = 80 ms
S phase
WT
nhp6Δ
MSD (μm)²
2.00
0.15
0.10
0.05
0.00
0
10
20
30
40
Δt (s)
PES4 locus
e
Constraining forces
loose
tight
MET10
NS
25
75
125
PES4
**
25
75
125
k_C (k_BT/μm²)
f
MET10 locus
Relative TetR-mCh volume
2.5
2.0
1.5
1.0
0.5
***
*
*
n= 356
n= 187
n= 325
n= 190
n= 154
n= 123
Asy.
G1
S

Figure 7

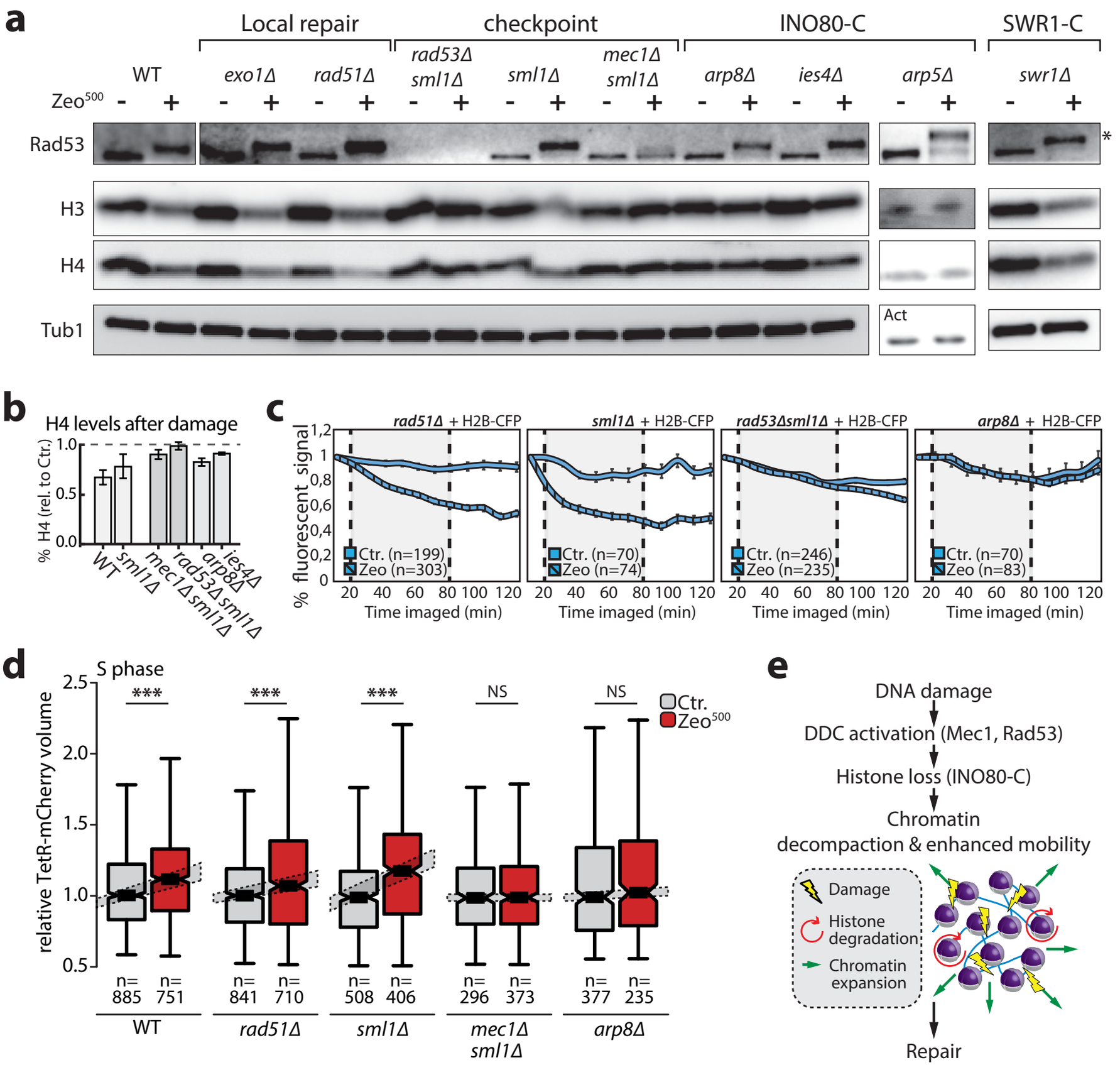
a
Local repair
checkpoint
INO80-C
SWR1-C
WT
exo1Δ
rad51Δ
rad53Δ sml1Δ
sml1Δ
mec1Δ sml1Δ
arp8Δ
ies4Δ
arp5Δ
swr1Δ
Zeo500 - + - + - + - + - + - + - + - + - + - +
Rad53
H3
H4
Tub1
Act
*
b
H4 levels after damage
% H4 (rel. to Ctr.)
1.0
0.5
0.0
WT
sml1Δ
mec1Δsml1Δ
rad53Δsml1Δ
arp8Δ
ies4Δ
c
rad51Δ + H2B-CFP
sml1Δ + H2B-CFP
rad53Δsml1Δ + H2B-CFP
arp8Δ + H2B-CFP
% fluorescent signal
1,2
1
0,8
0,6
0,4
0,2
0
Ctr. (n=199)
Zeo (n=303)
Ctr. (n=70)
Zeo (n=74)
Ctr. (n=246)
Zeo (n=235)
Ctr. (n=70)
Zeo (n=83)
20 40 60 80 100 120
Time imaged (min)
d
S phase
relative TetR-mCherry volume
2.5
2.0
1.5
1.0
0.5
***
***
***
NS
NS
Ctr.
Zeo500
n= 885 n= 751
n= 841 n= 710
n= 508 n= 406
n= 296 n= 373
n= 377 n= 235
WT
rad51Δ
sml1Δ
mec1Δ sml1Δ
arp8Δ
e
DNA damage
DDC activation (Mec1, Rad53)
Histone loss (INO80-C)
Chromatin
decompaction & enhanced mobility
Damage
Histone degradation
Chromatin expansion
Repair

Figure 8

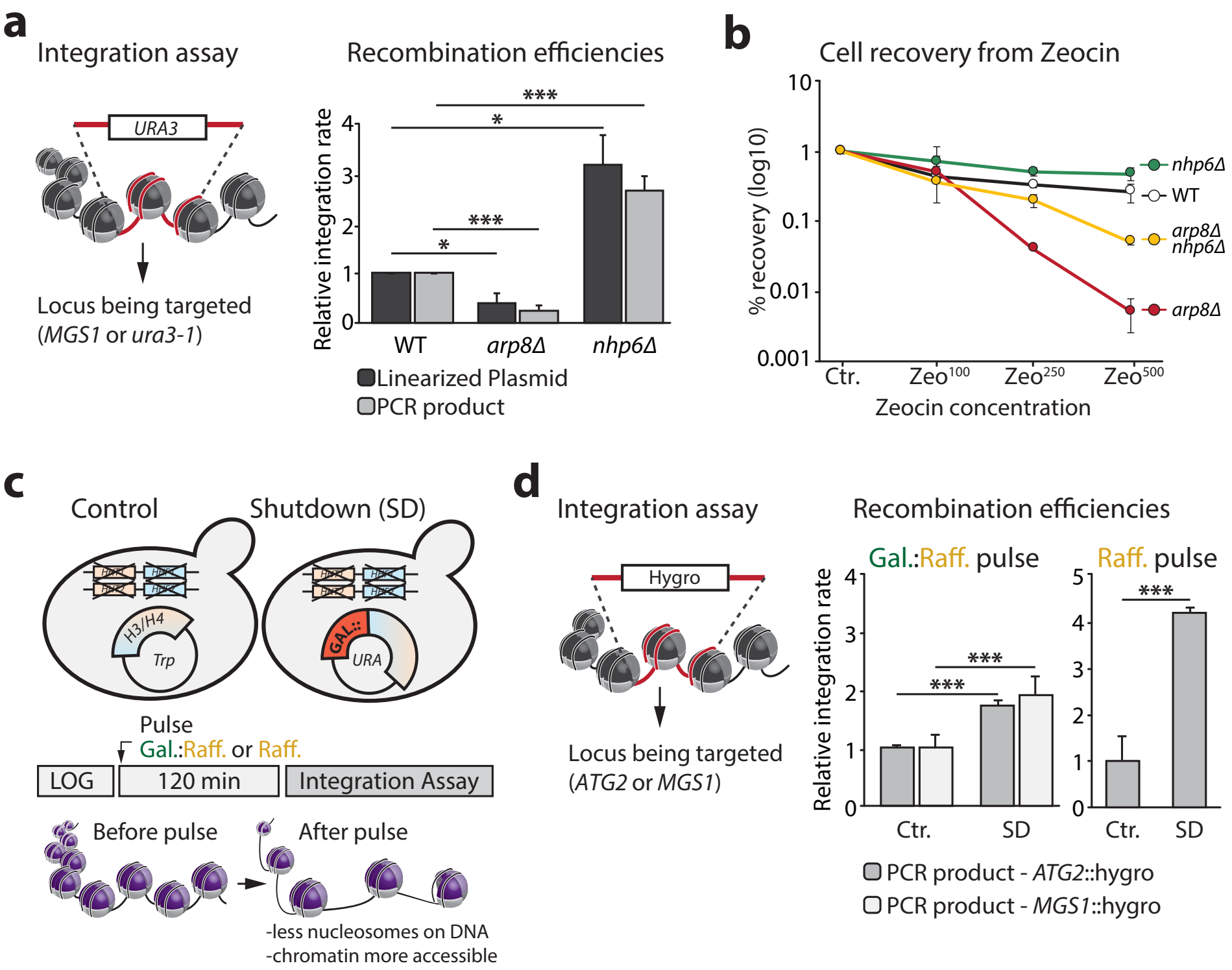
a
Integration assay
URA3
Locus being targeted
(MGS1 or ura3-1)
Recombination efficiencies
Relative integration rate
***
*
***
*
WT
arp8Δ
nhp6Δ
Linearized Plasmid
PCR product
b
Cell recovery from Zeocin
% recovery (log10)
nhp6Δ
WT
arp8Δ nhp6Δ
arp8Δ
Ctr.
Zeo100
Zeo250
Zeo500
Zeocin concentration
c
Control
Shutdown (SD)
H3/H4
Trp
GAL::
URA
Pulse
Gal.:Raff. or Raff.
LOG
120 min
Integration Assay
Before pulse
After pulse
-less nucleosomes on DNA
-chromatin more accessible
d
Integration assay
Hygro
Locus being targeted
(ATG2 or MGS1)
Recombination efficiencies
Gal.:Raff. pulse
Raff. pulse
Relative integration rate
***
***
***
Ctr.
SD
Ctr.
SD
PCR product - ATG2::hygro
PCR product - MGS1::hygro

Supplementary Items List

Note that we do NOT copy edit or otherwise change supplementary information, and minor (nonfactual) errors in these documents cannot be corrected after publication.
Please check carefully for errors.

Journal: Nature Structural & Molecular Biology

Article Tracking Number:	NSMB-A36792A
Article Title:	**Histone degradation in response to DNA damage enhances chromatin dynamics and recombination rates**
Corresponding Author:	Susan M. Gasser (Susan.gasser@fmi.ch)

Supplementary items submitted in combined files	
	Please enter numbers below
Number of Supplementary Figures submitted in Integrated Supplementary Figure template	7
Number of Supplementary Tables submitted in combined PDF file	4
Number of Supplementary Notes submitted in combined PDF file	1

Supplementary items submitted in additional files (e.g., Videos, Data Sets and Excel Tables)	
Please list items, titles and captions below, following the examples shown	
Supplementary Item & Number	**Title and Caption**
Supplementary Video 1	**H2B-CFP intensity decreases in response to DNA damage.** Visualization of data shown in **Fig. 1d**. Exemplary time course of 9 individual cells following H2B-CFP intensities after 60 min (20 min – 80 min time point) treatment with 300 µg/ml Zeocin for a total time of 120 min. Shown is a merge of Brightfield (average intensity projections) and CFP (maximum intensity projection) channels. Time-lapse series (120 min total) of 100 optical slices per stack (200nm intervals) were acquired for 12 time points at 10 min intervals, with each slice being exposed for 10 msec per laser line. Video was generated with Fiji (ImagJ) and is shown at 2 frames per second. Original Δt is shown in the top right corner.
Supplementary Video 2	**CFP-LacI, TetR-mRFP time-course used for live cell 3D inter-distance measurements.** Visualization of data shown in Fig. 4b.

	Exemplary time course of CFP-LacI and TetR-mRFP used for 3D inter-distance measurements in living cells. The fluorescent channels were acquired simultaneously on two different CCD cameras; taking 8 optical slices (200nm thickness) per stack every 300 ms for 2 min, with 10 ms exposure times per slice respectively. Video was generated using the Imaris 8.2.0 software and is shown at 25 frames per second (7.5x faster than the original acquisition speed).
Supplementary Dataset 1	**Uncropped Immunoblot images.** Uncropped blot images used in Fig. 1b, 2a, 2b, 2c and 7a
Supplementary Dataset 2	**Summary of mobility parameters.** Table showing the strains, conditions and mobility parameters.
Supplementary Dataset 3	**KNIME workflow.** File contains the KNIME workflow used for imaging data analysis.
Supplementary Dataset 4	**MS search results peptides table cycling cells label swap.** File contains MaxQuant search results used for quantifications.
Supplementary Dataset 5	**MS search results protein groups table cycling cells label swap.** File contains MaxQuant search results used for quantifications.
Supplementary Dataset 6	**MS search results peptides table cycling cells non label swap.** File contains MaxQuant search results used for quantifications.
Supplementary Dataset 7	**MS search results protein groups table cycling cells non label swap.** File contains MaxQuant search results used for quantifications.
Supplementary Dataset 8	**MS search results peptides table G1 arrest cells.** File contains MaxQuant search results used for quantifications.
Supplementary Dataset 9	**MS search results protein groups table G1 arrest cells.** File contains MaxQuant search results used for quantifications.

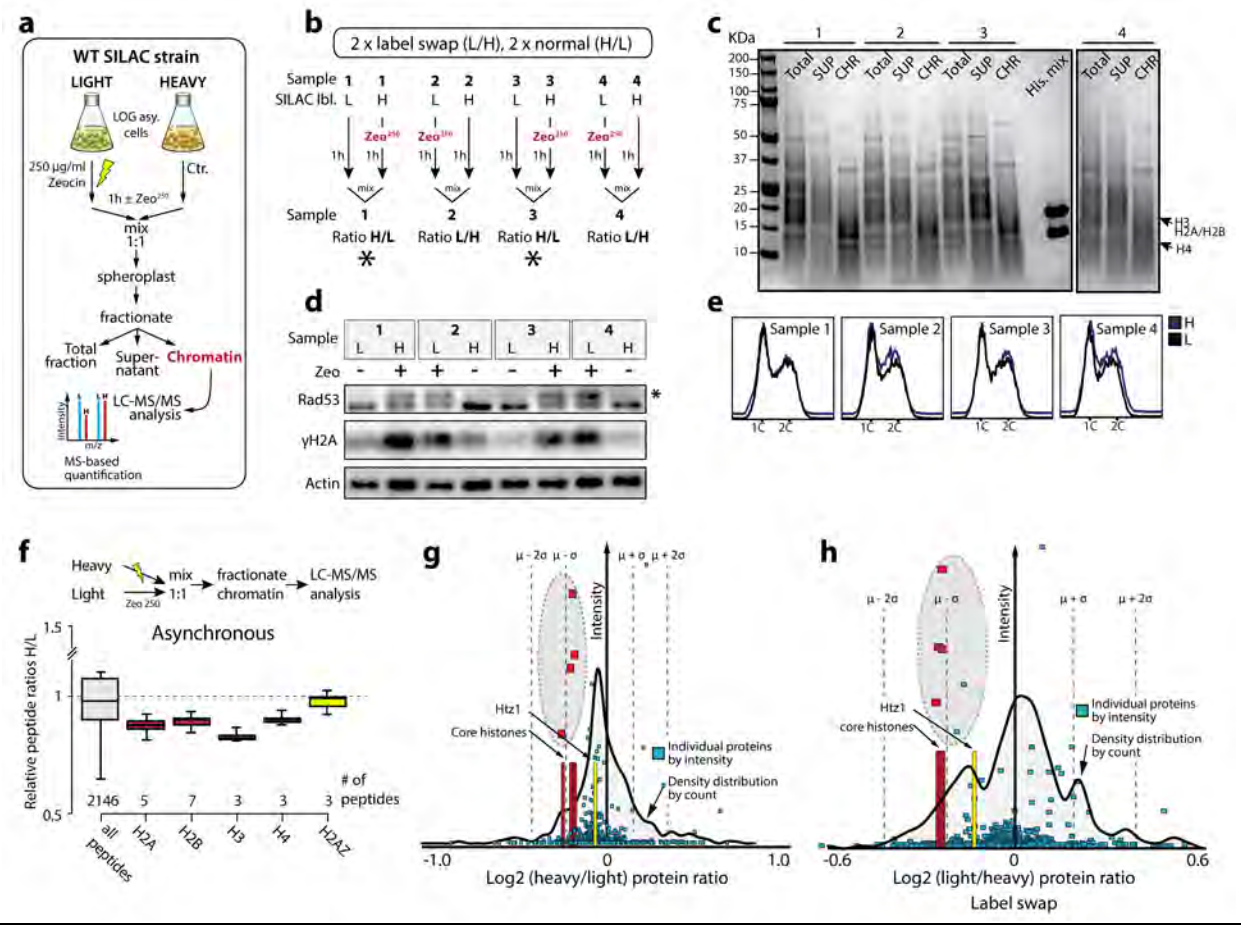

Supplementary Figure 1

SILAC mass spectrometry of pre-enriched chromatin depicts core histone loss

(**a**) Experimental workflow for SILAC mass spectrometry after Zeocin treatment. (**b**) Labeling and mixing of samples from 4 individual experiments. Asterisks indicates label swap (**c**) Colloidal Commassie stained SDS-PAGE of SILAC experiment replicas showing total protein, supernatant (SUP), and chromatin (CHR) fractions from **a**. His. mix is an equimolar mixture of recombinant Histone H2A, H2B, H3 and H4. (**d**) Control Immunoblot analysis using anti-γH2A anti-Rad53 antibodies to show that checkpoint is activated after Zeocin treatment in the SILAC samples from **bc. (e**) FACS analysis showing that all samples from **b-d** have similar cell cycle profiles. Actin was used as loading control. Asterisks indicate the phosphorylation-dependent mobility shift of Rad53. (**f**) SILAC mass spectrometry on chromatin fractions from three independent cell pools. Boxplots show heavy/light histone peptide distribution indicating the degradation of core histones and, to a lesser extent, Htz1 (H2A.Z). (**g**) Distribution of measured protein ratios in the non-label swap experiment or (**h**) label swap experiment. Core histones are labelled red and reside within the µ-σ range. Htz1 is labelled yellow resides closer to the mean ratio of all proteins. Boxplots in **f** represent median values, interquartile ranges and whiskers.

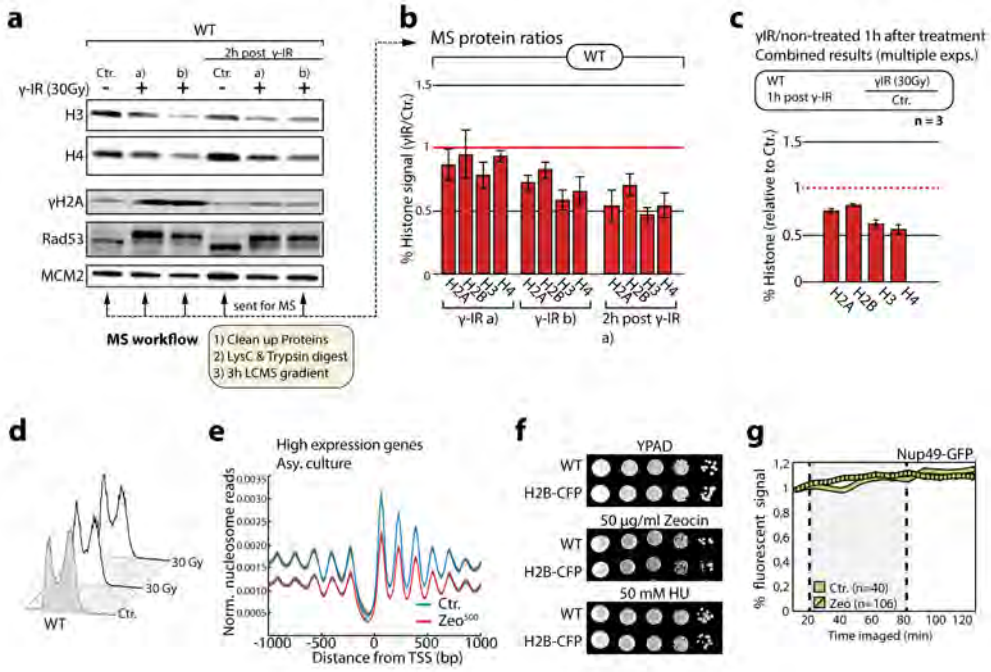

Supplementary Figure 2

Gamma radiation triggers degradation of core histones. Zeocin reduces nucleosome occupancy. H2B-CFP tagging does not interfere with cell viability

(**a**) Immunoblot analysis from one experiment using H3 and H4 specific antibodies on whole cell extracts of asynchronous WT cells exposed to 30 Gy gamma irradiation (γ-IR). Rad53 and γH2A were probed to confirm checkpoint activation. MCM2 was used to control for loading. Arrows indicate samples sent for label-free quantitative mass spectrometric analysis. (**b)** Label-free quantitative mass spectrometry results of samples depicted in **a**. Bar graphs show mean peptide ratios ± s.e.m for the indicated histone proteins upon γIR exposure relative to the control condition. (**c**) Combined label-free mass spectrometry results of sample γ-IR a), γIR b) and an additional experiment. Bar graphs represent the mean peptide ratios (γIR/Ctr.) ± s.e.m. for core histones over all samples. (**d**) FACS analysis showing that all samples have similar cell cycle profiles. (**e**) Genome-wide nucleosome mapping graph shows the distribution of nucleosome reads over 750 highly expressed genes aligned to their TSS from four independent experiments (±s.d. is shaded). (**f**) Drop assay control showing that the H3-CFP fusion complements the absence of H3 in response to genotoxic agents. (**g**) Live single-cell microscopy of Nup49-GFP. Graph shows the the mean fluorescent signals of of all individual cells (cell numbers indicated in graph) per treatment over time relative to the control (Ctr.) condition.

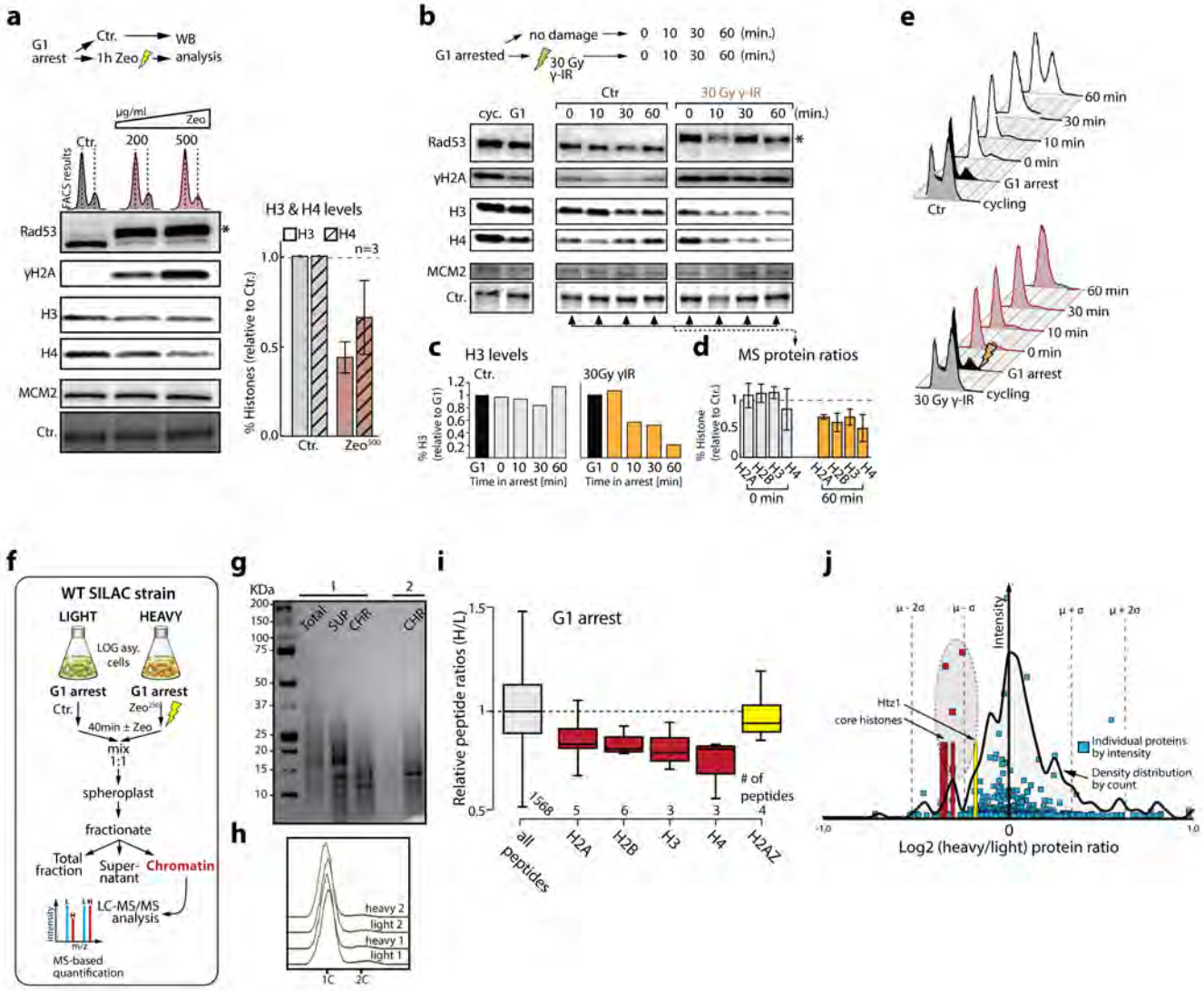

Supplementary Figure 3

Damage-induced histone loss occurs in G1 phase

(**a-b**) Representative immunoblot analysis of whole cell extracts from G1-arrested cells treated with Zeocin **a** or after exposure to γIR **b**. Histone H3 and H4 levels were probed using histone specific antibodies. Rad53 and γH2A were probed to confirm checkpoint activation. MCM2 was used to control for loading and Ctr. represents bands on the ponceau stained membrane. Bar graphs in **a** show the mean ± s.e.m. over three independent replicates relative to the control condition. FACS results of Zeocin treated samples are shown above immunoblots in **a**. Arrows in **b** indicate samples sent for label-free quantitative mass spectrometric analysis. (**c**) Immunoblot quantifications of irradiated samples from one experiment marked with arrows. (**d**) Label-free quantitative mass spectrometry results of samples depicted with arrows. Bar graphs show mean peptide ratios ± s.e.m. for the indicated histone proteins upon γIR exposure relative to the control condition. (**e**) FACS analysis showing cell cycle profiles of all samples from **b**. (**f**) Experimental workflow for SILAC mass spectrometry of G1 arrested cells after Zeocin treatment. (**g**) Commassie stained SDS-PAGE of samples showing total protein, supernatant (SUP), and chromatin (CHR) fractions. (**h**) FACS analysis showing similar G1 arrest efficiency for all samples. (**i**) SILAC mass spectrometry on chromatin fractions from two independent cells pools. Boxplots show heavy/light histone peptide distribution indicating the degradation of core histones and, to a lesser extent, Htz1 (H2A.Z). (**j**) Distribution of measured proteins ratios. Core histones are labelled red and reside within the µ-σ range. Htz1 (H2A.Z) is labelled yellow and residues closer to the mean ratio of all proteins. Boxplots in **i** represent median values, interquartile ranges and whiskers. Asterisk indicates phosphorylation-dependent Rad53 mobility shift.

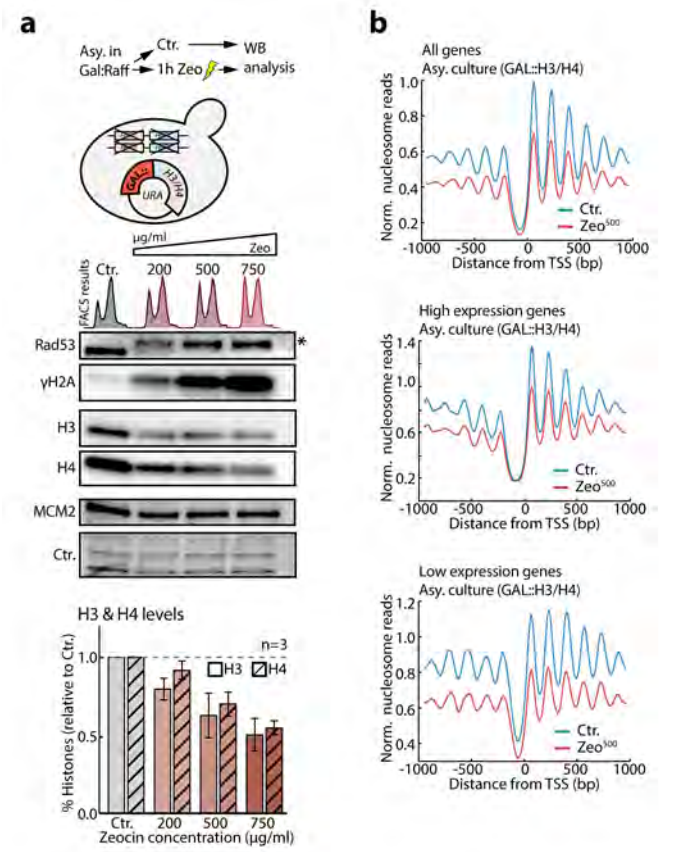

Supplementary Figure 4

Damage-induced histone loss is independent of histone transcription

(**a**) Top panel shows experimental procedure and strain schematic for constitutive histone H3 and H4 transcription in cells grown YPGal:Raff medium. A plasmid borne construct in which the GAL1/10 promoter drives the only pair of histone H3/H4 genes is used. Mid panel shows representative immunoblot analysis using anti-H3 and anti-H4 antibodies on whole cell extracts from the strain depicted in **a** after Zeocin treatment and growth in YPGal:Raff medium. Rad53 and γH2A were probed to confirm checkpoint activation. MCM2 was used to control for loading and Ctr. represents bands on the original gel (UV-TGX stained). Bar graphs in bottom panel show the mean ± s.e.m. over three independent replicates relative to the control condition. Asterisk indicates phosphorylation-dependent Rad53 mobility shift. (**b**) Zeocin treatment causes a genome-wide decrease in nucleosome occupancies. Data represents nucleosome occupancies over the total pool of 5014 protein coding genes, 750 high expression genes and 750 low expression genes aligned to their transcriptional start site (TSS) from one experiment using the strain depicted in **a**.

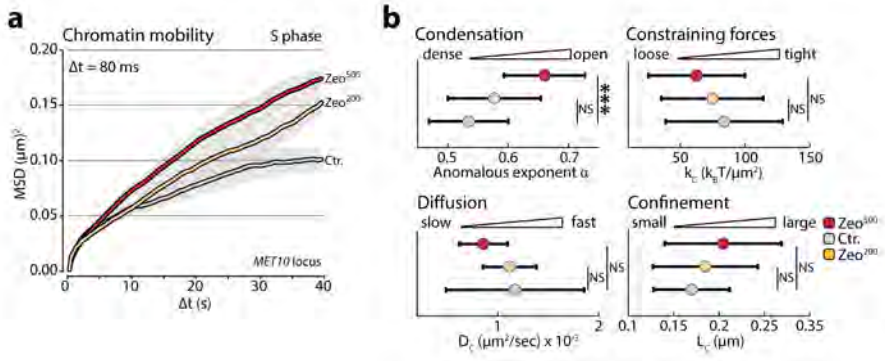

Supplementary Figure 5

High-speed, live cell imaging reveals increase in chromatin movement and loss of constraining forces following DNA damage

(**a**) High-speed (Δt=80 ms) imaging of the undamaged *MET10* locus (as in **Fig. 3a-b**) showing that chromatin mobility increases with Zeocin concentration. Average MSD graphs indicate dose-dependent increases in global chromatin mobility in response to DNA damage ($n^{Ctr.}$=39, n^{Zeo200}=31, n^{Zeo500}=29 different cells from three independent experiments). (**b)** Graphs show the medians and whiskers of biophysical parameters derived from imaging data and predict chromatin decompaction after Zeocin treatment. P-values, ***P<0.001, NS=not significant, result from Kolmogorow-Smirnow-tests. All MSD graphs represent the mean ± s.e.m. of cells pooled from three independent experiments. Additionally, consult Supplementary Dataset 2 for mobility parameters and the number of cells analyzed.

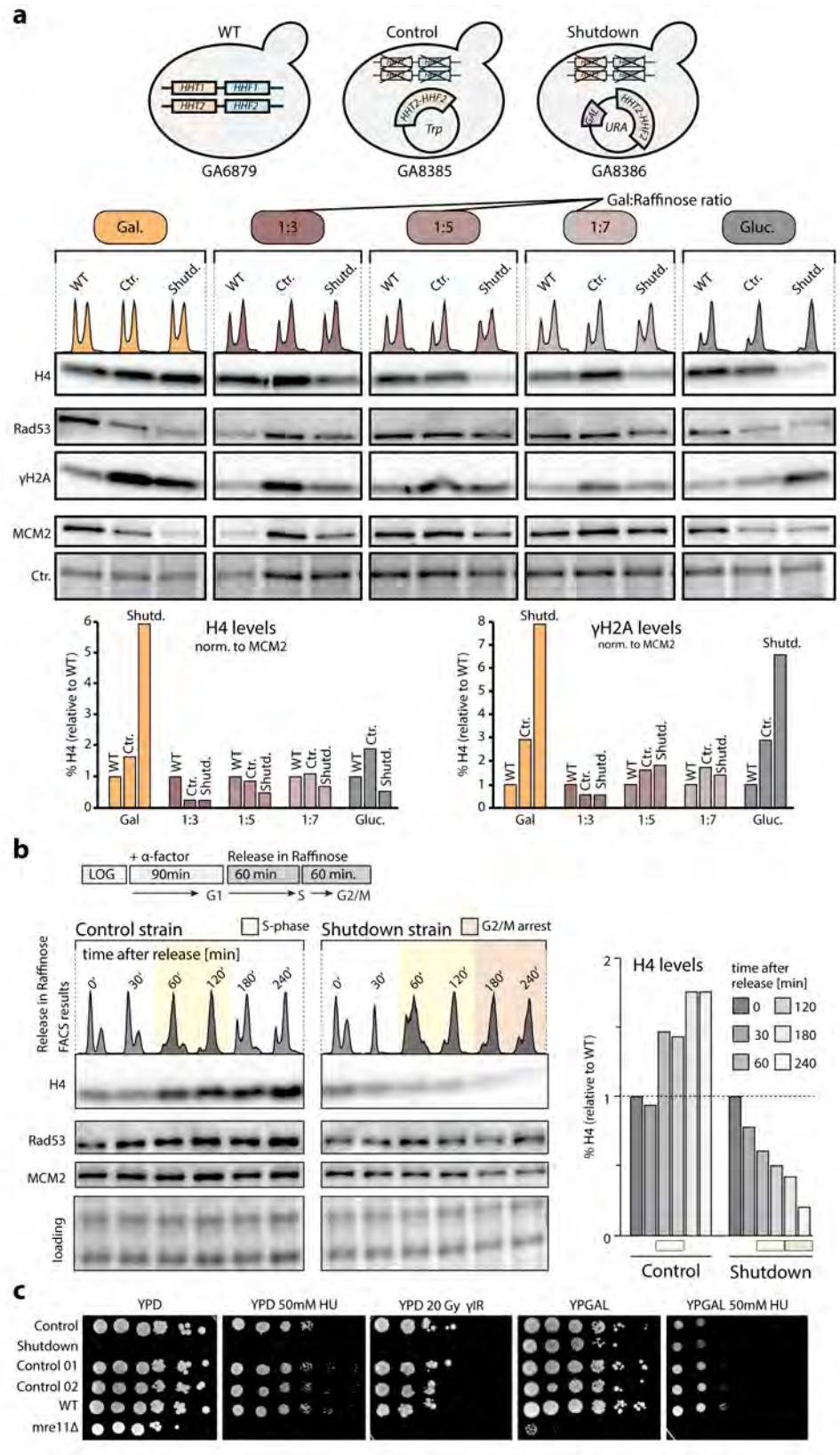
a
WT
Control
Shutdown
HHT1
HHF1
HHT2
HHF2
HHT2-HHF2
Trp
GAL
URA
GA6879
GA8385
GA8386
Gal:Raffinose ratio
Gal.
1:3
1:5
1:7
Gluc.
WT
Ctr.
Shutd.
H4
Rad53
γH2A
MCM2
Ctr.
H4 levels
norm. to MCM2
% H4 (relative to WT)
γH2A levels
b
+ α-factor
Release in Raffinose
LOG
90min
60 min
60 min.
G1
S
G2/M
Control strain
S-phase
Shutdown strain
G2/M arrest
time after release [min]
Release in Raffinose
FACS results
loading
time after release [min]
Control
Shutdown
c
YPD
YPD 50mM HU
YPD 20 Gy γIR
YPGAL
YPGAL 50mM HU
Control
Shutdown
Control 01
Control 02
WT
mre11Δ

Supplementary Figure 6

GAL::H3/H4 strain as a tool for *in-vivo* artificially controlled histone level reductions

(**a**) Schematic representation of wild-type, control and shutdown strains grown in the indicated media. Gal. = galactose, gluc. = glucose. Immunoblot analysis of whole cell extracts of the indicated conditions and strains were performed using an antibody directed against Histone H4. Rad53 and γH2A were probed to confirm checkpoint activation. MCM2 was used to control for loading. Bar graphs from quantified immunoblot derived from one experiment shows overexpression or reduction of H3/H4 in the shutdown strain grown in gal. or gluc. medium respectively. Growth of the shutdown strain in Gal:Raff 1:5 confers H3/H4 levels similar to WT. (**b**) Experimental workflow of the arrest-release experiment used to reduce histone levels in S phase (as in **Fig. 5**). Bar graphs from quantified immunoblot data derived from one experiment shows reductions of H3 and H4 upon release into raffinose medium. (**c**) A defined number of exponentially growing cells (fivefold dilutions) was spotted on different YP or YPD plates containing the indicated dose of hydroxyurea (HU). Cells exposed to 20 Gy γIR were spotted onto YPD plates. Drop assays show functionality of shutdown and control strains. Control = control from **a**, control 1 and 2 = similar to control 1 but expressing HHT2-HHF2 from a URA plasmid.

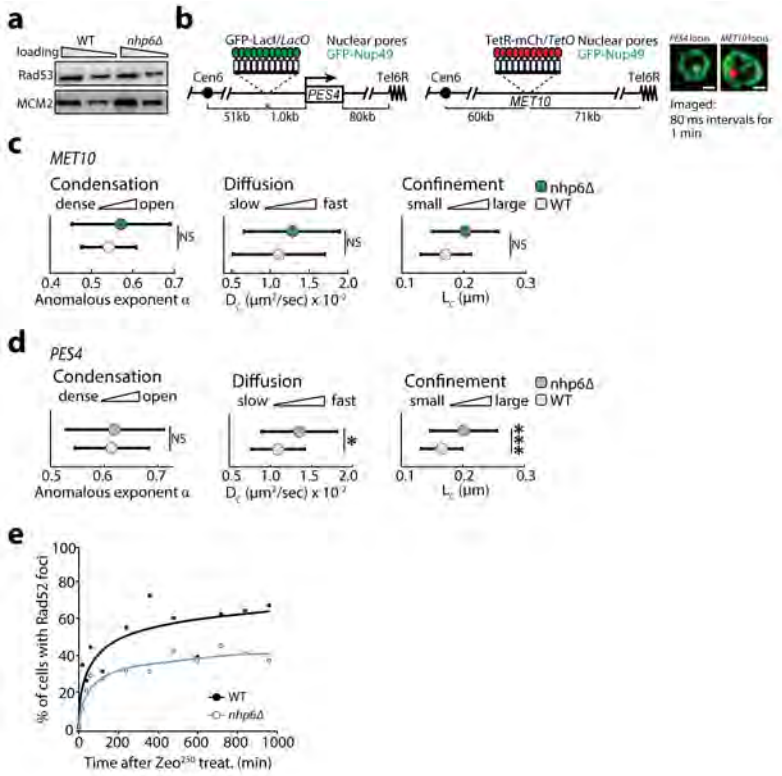

Supplementary Figure 7

Biophysical parameters of *nhp6*Δ tracking data and results from Rad52-YFP recovery assay

(**a**) Control Immunoblot from one experiment (loading 1x and 2x the volume) showing that *nhp6Δ* strains do not have constitutive checkpoint activation. Rad53 was probed to test for checkpoint activation and MCM2 was used as loading control. (**b**) Schematics of the strains used for imaging the *PES4* and *MET10* loci (**Fig. 6c-e**) with representative images. Scale bar is 2 µm. (**c-d**) Graphs show the medians and whiskers of biophysical parameters derived from imaging data of *PES4* **c** and *MET10* **d** (**Fig. 6c,d**). P-values, P*P<0.05, ***P<0.001, NS=not significant, result from Kolmogorow-Smirnow-Tests. (**e**) Rad52-YFP foci recovery assay. Graph shows the overall percentage of Rad52-YFP foci containing cells for each of the 12 time-points from one experiment plotted against the time and shown together with a logarithmic fit.

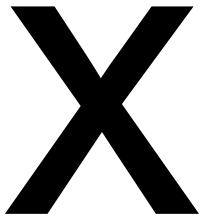

Supplementary Figure 8

Insert figure title here by deleting or overwriting this text; keep title to a single sentence; use Symbol font for symbols and Greek letters.

Insert figure caption here by deleting or overwriting this text; captions may run to a second page if necessary. To ensure accurate appearance in the published version, please use Symbol font for all symbols and Greek letters.

Supplementary Tables

Nucleosome mapping sequencing reads

Supplementary Table 1: Information on sequencing reads obtained for each nucleosome mapping replicate. The strain column indicates the strains used. GA-6879 is the wild type and GA-8386 the shutdown strain grown in galactose:raffinose medium. A-C in the strain column indicates the four independent experiments with or without Zeocin treatment for 1h prior to MNase digestion. Column A shows the *S. Cerevisiae* reads and column B the reads from the *C. glabrata* spike-in control.

	A	B	C=(A+B)	E=(A/C)	F=(B/C)*100
Strain	***S. ce.***	***C. glab.***	**total**	**Read fraction *S. cer.***	**Read fraction *C. glab.***
GA-6879_A	50692473.00	9866228.00	60558701.00	0.84	0.16
GA-6879_A_Zeocin	46090144.00	13483686.00	59573830.00	0.77	0.23
GA-6879_B	38787017.00	7282715.00	46069732.00	0.84	0.16
GA-6879_B_Zeocin	36619974.00	10714730.00	47334704.00	0.77	0.23
GA-6879_C	34427922.00	6626795.00	41054717.00	0.84	0.16
GA-6879_C_Zeocin	29746798.00	7722737.00	37469535.00	0.79	0.21
GA-6879_D	25931187.00	4679458.00	30610645.00	0.85	0.15
GA-6879_D_Zeocin	43185379.00	12185328.00	55370707.00	0.78	0.22
GA-8386_A	82089867.00	21788485.00	103878352.00	0.79	0.21
GA-8386_A_Zeocin	53677477.00	20342128.00	74019605.00	0.73	0.27
GA-8386_B	41546073.00	9859227.00	51405300.00	0.81	0.19
GA-8386_B_Zeocin	32786223.00	12332953.00	45119176.00	0.73	0.27
GA-8386_C	25328106.00	6741373.00	32069479.00	0.79	0.21
GA-8386_C_Zeocin	27560758.00	10640545.00	38201303.00	0.72	0.28
GA-8386_D	30336089.00	7284044.00	37620133.00	0.81	0.19
GA-8386_D_Zeocin	31958581.00	12219914.00	44178495.00	0.72	0.28

Yeast strains used in this study

Supplementary Table 2: Yeast strains used in this study. All strains are haploid and all except the SILAC strain and the Htz1-mEos imaging control are derived from the W303 background.

Strain number	Genotype	Source
BY	*MAT**a***; *his3del200*; *leu2del0*; *met15del0*; *trp1del63*; *ura3del0*; (BY4733)	exemplary genotype
W303	*MAT**a***; *ade2-1*; *trp1-1*; *his3-11*; *his3-15*; *ura3-1*; *leu2-3*; *leu2-112*; (W303)	exemplary genotype
JKM179	*MAT**α***; *hml::ADE1*; *hmr::ADE1*; *ade3::GALHO*; *leu2-3*; *lys5 trp1::hisG*; *ura3-52* (JKM179)	exemplary genotype
yAG-06A	*YHR018c::kanMX4*; *YIR034c::kanMX4* (BY4733)	[1]
GA-6879	*MAT**a**, RAD52-YFP*; *NUP49-GFP*; *ADE2::TetR-mCherry*; *lys5::LacI-CFP::TRP*; *leu2::LoxP*; *ZWF1:cutsite(Lmn::lys5::IsceIcs::LEU2::LacO array::Lmn)*; *met10::lmn adaptamers::HIS3::TetOps-LexA* (W303)	[2]
GA-9773	*MAT**a***; *PES4::4xLexA-lacO::TRP1*; *his3-15::GFP-LacI-HIS3*; *NUP49-GFP*	This study
GA-9774	*nhp6a::kanMX4*; *nhp6b::kanMX4*, same as GA-9773	This study
GA-9771	*nhp6a::kanMX4*; *nhp6b::kanMX4*, same as GA-6879	This study
GA-9815	*arp8::NAT,* same as GA9771	
GA-9772	Isogenic to GA-6879	This study
GA-7553	*sml1::HIS3*; same as GA-6879	This study
GA-8132	arp8::NAT; same as GA-6879	This study
GA-8182	ies4::NAT; same as GA-6879	This study
GA-8185	swr1::NAT; same as GA-6879	This study
GA-8202	arp5::NAT; same as GA-6879	This study
GA-7551	*rad51::NAT*; in GA-6879	This study
GA-7552	*rad53::NAT*; same as GA-7553	This study
GA-7556	*mec1::NAT*; same as GA-7553	This study
GA-8385	*MAT**a***; *Nup49-GFP*; *GFP-LacI::HIS3*; *hht2-hhf2Δ hht1-hhf1Δ(no marker) + [#3495 pDM18 pRS415*; *HHT2-HHF2*; *CEN/ARS, TRP1]* (W303)	This study
GA-8386	*MAT**a***; *Nup49-GFP*; *GFP-LacI::HIS3*; *hht2-hhf2Δ hht1-hhf1Δ(no marker) + [#3484 pRM102 pUK420*; *GAL10-HHT2 GAL1-HHF2*; *CEN/ARS, URA3]* (W303)	This study
GA-8387	*MAT**a***; *Nup49-GFP*; *GFP-LacI::HIS3*; *hht2-hhf2Δ hht1-hhf1Δ(no marker) + [#3494 pDM9 pRS416*; *HHT1-HHF1*; *CEN/ARS*; *URA3]* (W303)	This study
GA-9775	*LacO::LEU2::MGS1*, same as GA8385	This study
GA-9776	*LacO::LEU2::MGS1*, same as GA8386	This study
GA-3364	*MAT**a***; *HTB2-CFP::kanXM* (W303)	Brian Luke
GA-9700	*rad51::URA3*; same as GA-3364	This study
GA-9698	*sml1::URA3*; same as GA-3364	This study
GA-9695	*arp8::natMX*; same as GA-3364	This study
GA-9712	*Rad53::natMX*; same as GA-9712	This study
GA-9594	*MAT**α***; *Htz1-Eos::URA3*; same as JKM179	This study
GA-5816	*MAT**α***; *Rad52-YFP*; *NUP49-GFP*; *HIS3::LacI-GFP* (W303)	This study
YMB08 (GA-9227)	*MAT**α***; *ura3-1::LacI-GFP-URA3*; *515kb-XIV::lacO-TRP1*; *YGL117::tetR-mRFP-NATMX*; *196kb-XIV::tetO-LEU2* (W303)	Kerstin Bystricky
GA-9777	*MAT**α***; *YGL117(ARS714)::TetR-mRFP-NAT*; *ade2-1::His3p-CFP-lacI-URA3p-LambdacI-YFP-ADE2*; *leu2-3,112 :: tetO-LEU2*; *74kb :: LambdaO-HIS3*; *40kb :: LacO-TRP1*; *RAD52-EGFP-CaURA3*	This study
GA-1365	*MAT**a**, pre1-1, pre2-2*	[3]
GA-1366	*Mat**a**,* WT strain isogenic to GA-1365 and GA-1366	[3]
GA-1364	*Mat**a**, erg6::LEU2*	[4]

Plasmids used in this study

Supplementary Table 3: Plasmids used in this study

Plasmid number	Description	Type	Yeast selection	Bacterial selection	Source
#3484	pUK420-GAL10-HHT2 GAL1-HHF2	CEN/ARS	URA3	AMP	Addgene [5]
#3494	pRS416-HHT1-HHF1	CEN/ARS	URA3	AMP	[6]
#3495	pRS414-HHT2-HHF2	CEN/ARS	TRP1	AMP	[7]
#279	pRS406	integrating	URA3	AMP	Addgene
#1049	pAG32	see source	see source	see source	[8]
#1050	pAG60	see source	see source	see source	[8]
#2422	pWJ132-hphMX4-Gal1-10	2µ plasmid	ADE2/hphMX4	AMP	This study

Antibodies used in this study

Supplementary Table 4: Antibodies used in this study

Antibody	Supplier	Conditions used
Mouse α Rad53	Custom made antibody (GenScript)	1:200 in milk
Rabbit α H4	Abcam AB 10158	1:5000 or 1:7500 in BSA
Mouse α actin	MAB1501	1:10,000 in milk
Goat α MCM2	Santa Cruz (SC 6680)	1:3000 in BSA
Rabbit α γH2A	Custom made antibody	1:3000 i BSA
Rabbit α H3	Abcam AB1791	1:10,000 in BSA
Rabbit α Ubiquitin	Abcam (AB19247)	1:2000 in milk

Supplementary Table References

1. Gruhler, A. et al. Quantitative phosphoproteomics applied to the yeast pheromone signaling pathway. *Mol Cell Proteomics* **4**, 310-27 (2005).
2. Seeber, A., Dion, V. & Gasser, S.M. Checkpoint kinases and the INO80 nucleosome remodeling complex enhance global chromatin mobility in response to DNA damage. *Genes Dev* **27**, 1999-2008 (2013).
3. Richterruoff, B., Wolf, D.H. & Hochstrasser, M. Degradation of the Yeast Mat-Alpha-2 Transcriptional Regulator Is Mediated by the Proteasome. *Febs Letters* **354**, 50-52 (1994).
4. Heese-Peck, A. et al. Multiple functions of sterols in yeast endocytosis. *Mol Biol Cell* **13**, 2664-80 (2002).
5. Mann, R.K. & Grunstein, M. Histone H3 N-terminal mutations allow hyperactivation of the yeast GAL1 gene in vivo. *EMBO J* **11**, 3297-306 (1992).
6. Duina, A.A. & Winston, F. Analysis of a mutant histone H3 that perturbs the association of Swi/Snf with chromatin. *Molecular and Cellular Biology* **24**, 561-572 (2004).
7. Park, J.H., Cosgrove, M.S., Youngman, E., Wolberger, C. & Boeke, J.D. A core nucleosome surface crucial for transcriptional silencing. *Nature Genetics* **32**, 273-279 (2002).
8. Goldstein, A.L. & McCusker, J.H. Three new dominant drug resistance cassettes for gene disruption in Saccharomyces cerevisiae. *Yeast* **15**, 1541-1553 (1999).

Supplementary Notes

Estimating the anomalous diffusion exponent α and the diffusion coefficient

We computed the cross-correlation (CC) function using [1]:

$$C(t) = \frac{1}{N_p - t} \sum_{k=1}^{N_p - t} (\mathbf{R}_c(k\Delta t) - \mathbf{R}_c((k+t)\Delta t)^2, \tag{6}$$

for $t = 1, T-1$, where N_p is the number of points in the trajectory. In many studies the CC is referred to as the MSD function [2,3] although these two functions are distinct[1]. The MSD is defined as the squared displacement with respect to the initial trajectory position, averaged over time:

$$\text{MSD(t)} = \left\langle \left(R_c(t) - R_c(0) \right)^2 \right\rangle.$$

For short times, $C(t)$ increases as a power law

$$C(t) = Ct^{\alpha}. \tag{7}$$

where $C > 0$. To extract the coefficient α, we computed $C(t)$ from empirical trajectories and fitted the first seven points of the curve to a power law. A chromatin or DNA locus is characterized experimentally by $\alpha < 1$ [4,5], while for normal diffusion $\alpha = 1$. In the Rouse polymer model[6], the anomalous exponent is $\alpha = 0.5$ computed for intermediate time regime (see [6]).

To compute the diffusion coefficient of the tagged monomer, we use the following empirical estimator described in [1]:

$$D_c = \frac{1}{4\Delta t} \sum_{k=1}^{N_p - 1} (\mathbf{R}_c(k\Delta t) - \mathbf{R}_c((k+1)\Delta t))^2, \tag{8}$$

For short time interval $\Delta t = b^2/D$, the locus motion is Brownian and the diffusion coefficient is well approximated by eq.(8).

Estimating the effective spring coefficient k_c

Because the chromatin interacts locally with its environment, we estimated this interaction using a polymer model[7], by a harmonic well of strength k acting on a single monomer $\mathbf{R}_n$. The potential energy of the interaction is

$$U(\mathbf{R}_n) = \frac{1}{2}k(\mathbf{R}_n - \boldsymbol{\mu})^2, \tag{9}$$

where $\boldsymbol{\mu}$ is the fix position of the interaction. The velocity of an observed monomer c, averaged over many trajectories is driven by this interacting force, following the relation described in [7]:

$$\lim_{\Delta t \to 0} E\{\frac{\mathbf{R}_c(t+\Delta t) - \mathbf{R}_c(t)}{\Delta t} \mid \mathbf{R}_c(t) = \mathbf{x}\} = -Dk_{cn}(\mathbf{x} - \boldsymbol{\mu}), \tag{10}$$

where $\mathbf{R}_c(t)$ is the position of locus c at time t and D the diffusion coefficient and $E\{. \mid \mathbf{R}_c(t) = \mathbf{x}\}$ means averaging over trajectory realizations such that the condition $\mathbf{R}_c(t) = \mathbf{x}$ is satisfied. Relation (18) links the average velocity of the observed monomer c to the force applied at a distance $|c - n|$. For a Rouse polymer, with a potential well of type (17), the effective spring coefficient is given by

$$k_{cn} = \frac{k\kappa}{\kappa + |c - n|k}, \tag{11}$$

where κ is the monomer-monomer spring coefficient. We estimated k_c from the empirical locus trajectories $\mathbf{R}_c(t)$ by

$$k_c \approx \frac{1}{2(N_p - 1)} \sum_{i=1}^{2} \sum_{h=1}^{N_p - 1} \frac{R_c^i((h+1)\Delta t) - R_c^i(h\Delta t)}{D_c \Delta t (R_c^i(h\Delta t) - \langle R_c^i \rangle)}, \tag{12}$$

where i is the spatial direction (in two dimensions, we sum over the x and y components) and N_p is the number of points in the trajectory. In practice, the quantity $\langle R_c^i \rangle$ is computed by averaging over the trajectory. The diffusion coefficient D_c can be computed by using eq. 8.

Supplementary Notes References

1. Schuss, Z. Diffusion and Stochastic Processes. An Analytical Approach. *Springer-Verlag, New York, NY* (2009).
2. Dion, V., Kalck, V., Horigome, C., Towbin, B.D. & Gasser, S.M. Increased mobility of double-strand breaks requires Mec1, Rad9 and the homologous recombination machinery. *Nat Cell Biol* **14**, 502-9 (2012).
3. Mine-Hattab, J. & Rothstein, R. Increased chromosome mobility facilitates homology search during recombination. *Nat Cell Biol* **14**, 510-7 (2012).
4. Kepten, E., Bronshtein, I. & Garini, Y. Improved estimation of anomalous diffusion exponents in single-particle tracking experiments. *Physical Review E* **87**(2013).
5. Weber, S.C., Theriot, J.A. & Spakowitz, A.J. Subdiffusive motion of a polymer composed of subdiffusive monomers. *Phys Rev E Stat Nonlin Soft Matter Phys* **82**, 011913 (2010).
6. Doi, M., Edwards, S. F. The Theory of Polymer Dynamics. . *Oxford: Clarendon Press.* (1986).
7. Amitai, A., Toulouze, M., Dubrana, K. & Holcman, D. Analysis of Single Locus Trajectories for Extracting In Vivo Chromatin Tethering Interactions. *PLoS Computational Biology* **11**, e1004433 (2015).

Fig. 1b

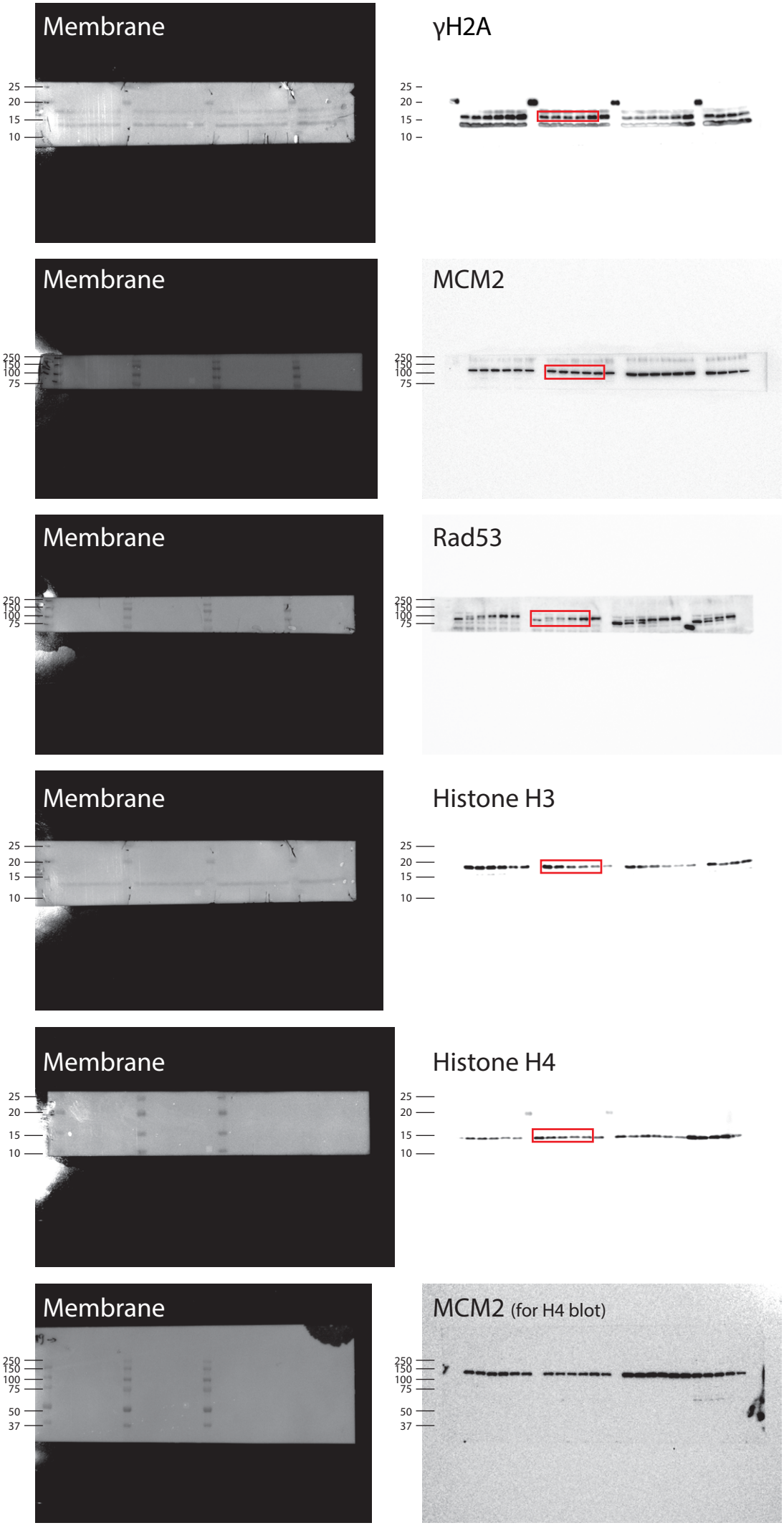
Membrane
γH2A
Membrane
MCM2
Membrane
Rad53
Membrane
Histone H3
Membrane
Histone H4
Membrane
MCM2 (for H4 blot)

Fig. 1b

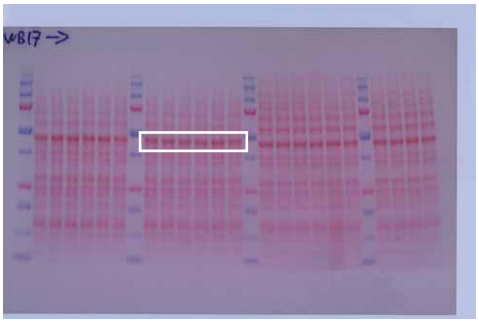

Ponceau stained membrane after transfer

Fig. 2a

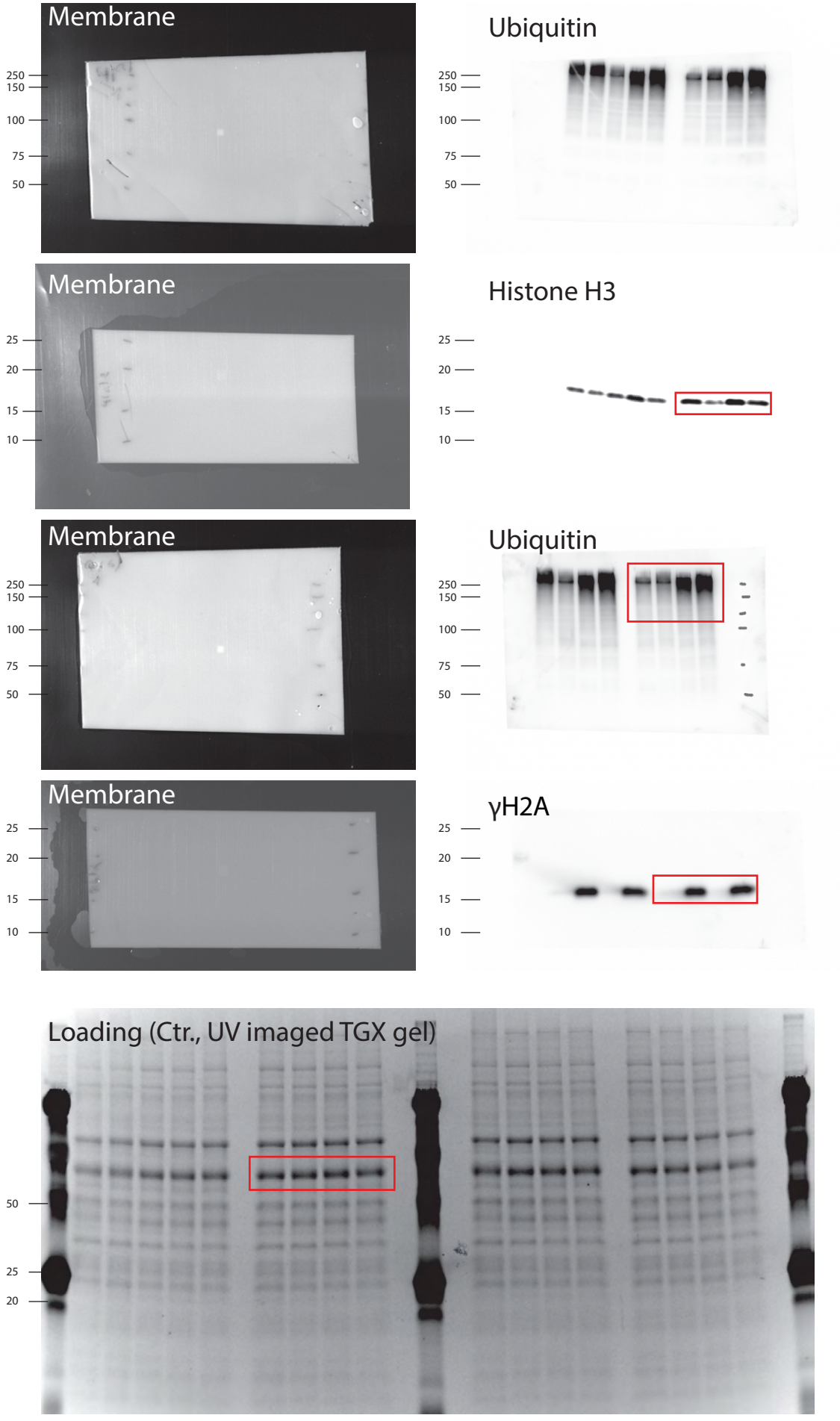
Membrane
250
150
100
75
50
Ubiquitin
250
150
100
75
50
Membrane
25
20
15
10
Histone H3
25
20
15
10
Membrane
250
150
100
75
50
Ubiquitin
250
150
100
75
50
Membrane
25
20
15
10
γH2A
25
20
15
10
Loading (Ctr., UV imaged TGX gel)
50
25
20

Fig. 2b

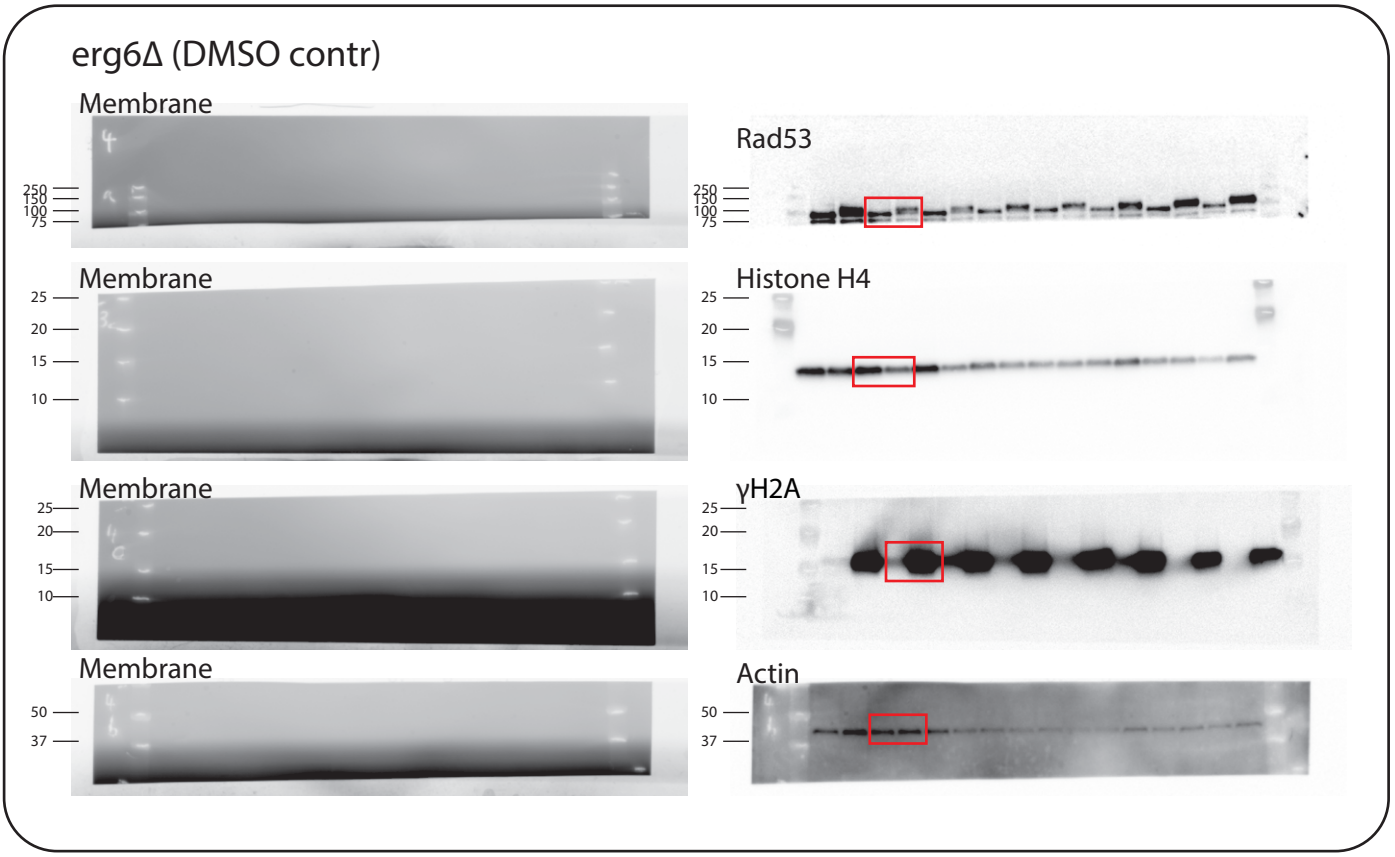
erg6Δ (DMSO contr)
Membrane
250
150
100
75
Rad53
Membrane
25
20
15
10
Histone H4
Membrane
γH2A
Membrane
50
37
Actin

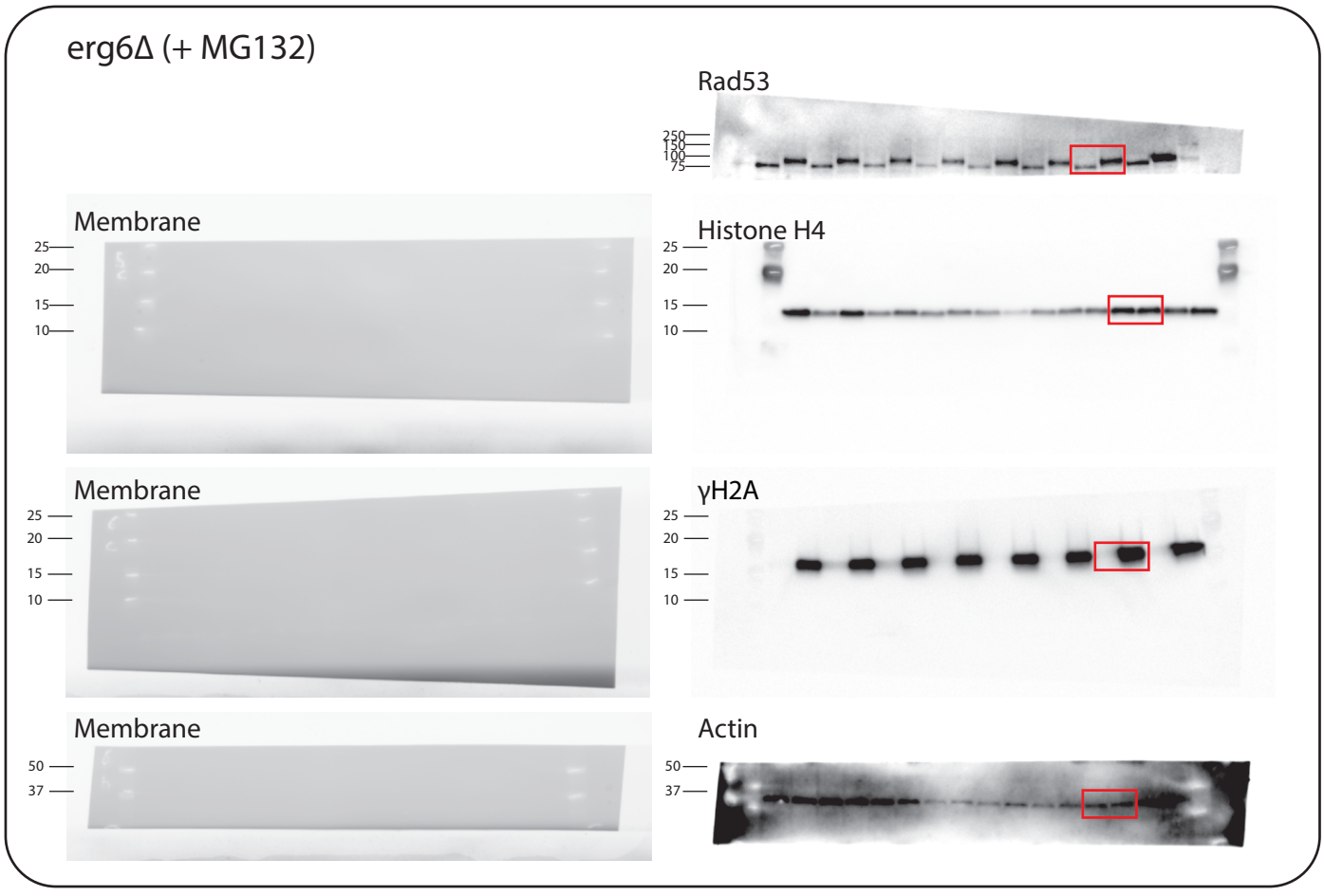
erg6Δ (+ MG132)
Rad53
Membrane
Histone H4
Membrane
γH2A
Membrane
Actin

Fig. 2c

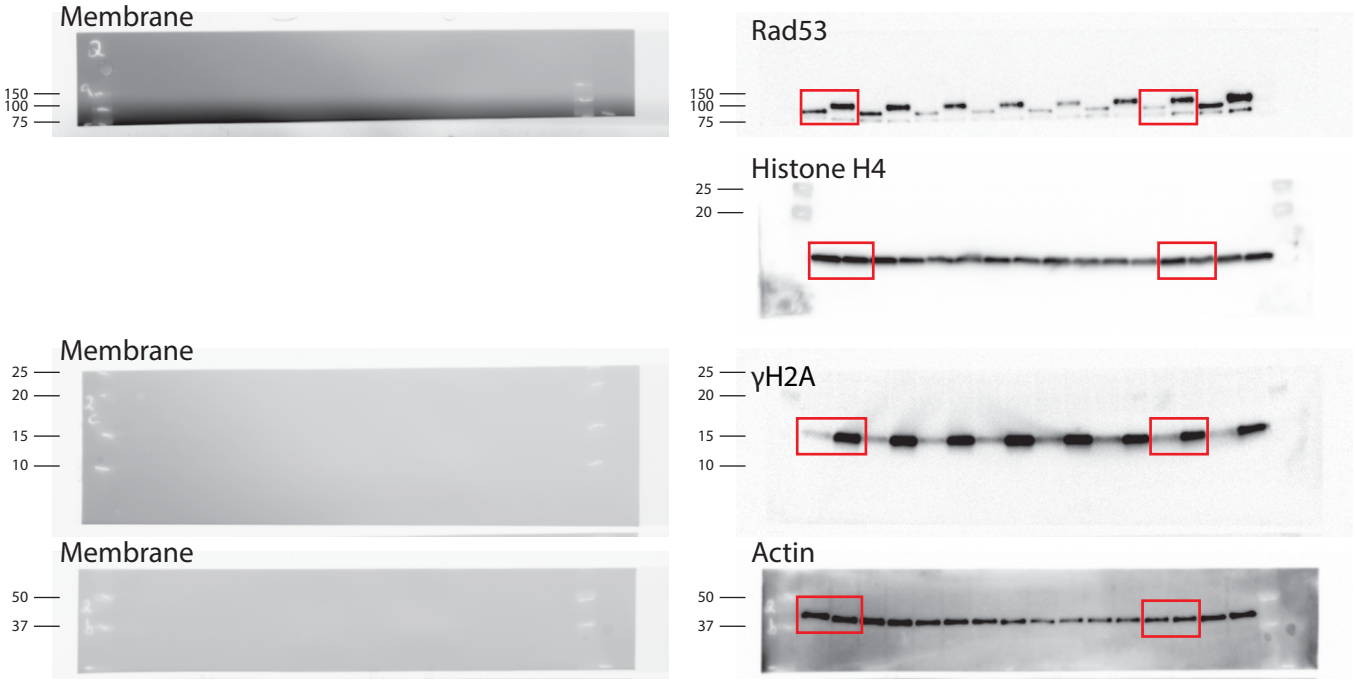
Membrane
150
100
75
Rad53
150
100
75
Histone H4
25
20
Membrane
25
20
15
10
γH2A
25
20
15
10
Membrane
50
37
Actin
50
37

Fig. 7a

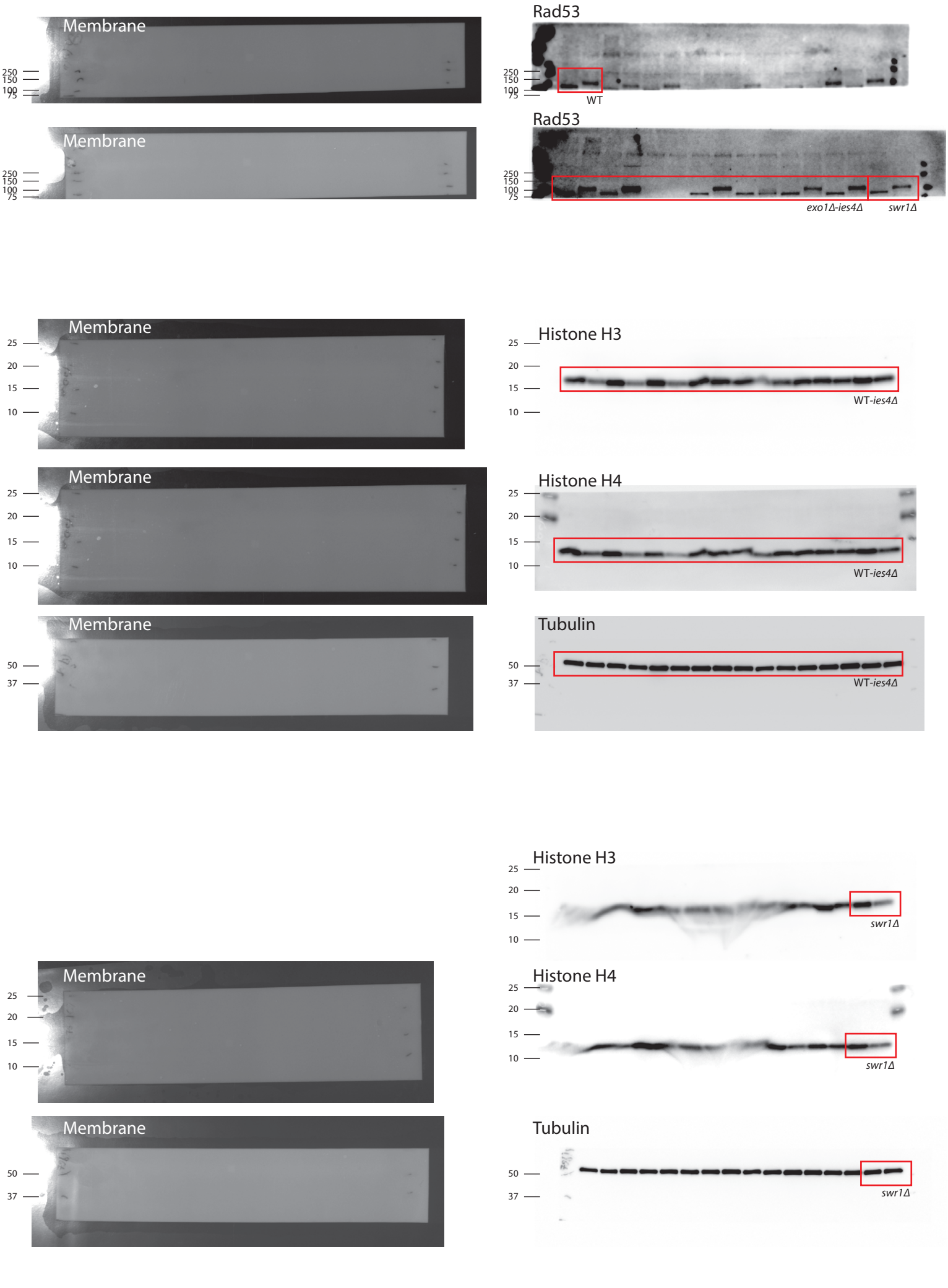
Membrane
250
150
100
75
Membrane
250
150
100
75
Rad53
250
150
100
75
WT
Rad53
250
150
100
75
exo1Δ-ies4Δ
swr1Δ
Membrane
25
20
15
10
Histone H3
25
20
15
10
WT-ies4Δ
Membrane
25
20
15
10
Histone H4
25
20
15
10
WT-ies4Δ
Membrane
50
37
Tubulin
50
37
WT-ies4Δ
Histone H3
25
20
15
10
swr1Δ
Membrane
25
20
15
10
Histone H4
25
20
15
10
swr1Δ
Membrane
50
37
Tubulin
50
37
swr1Δ

Fig. 7a

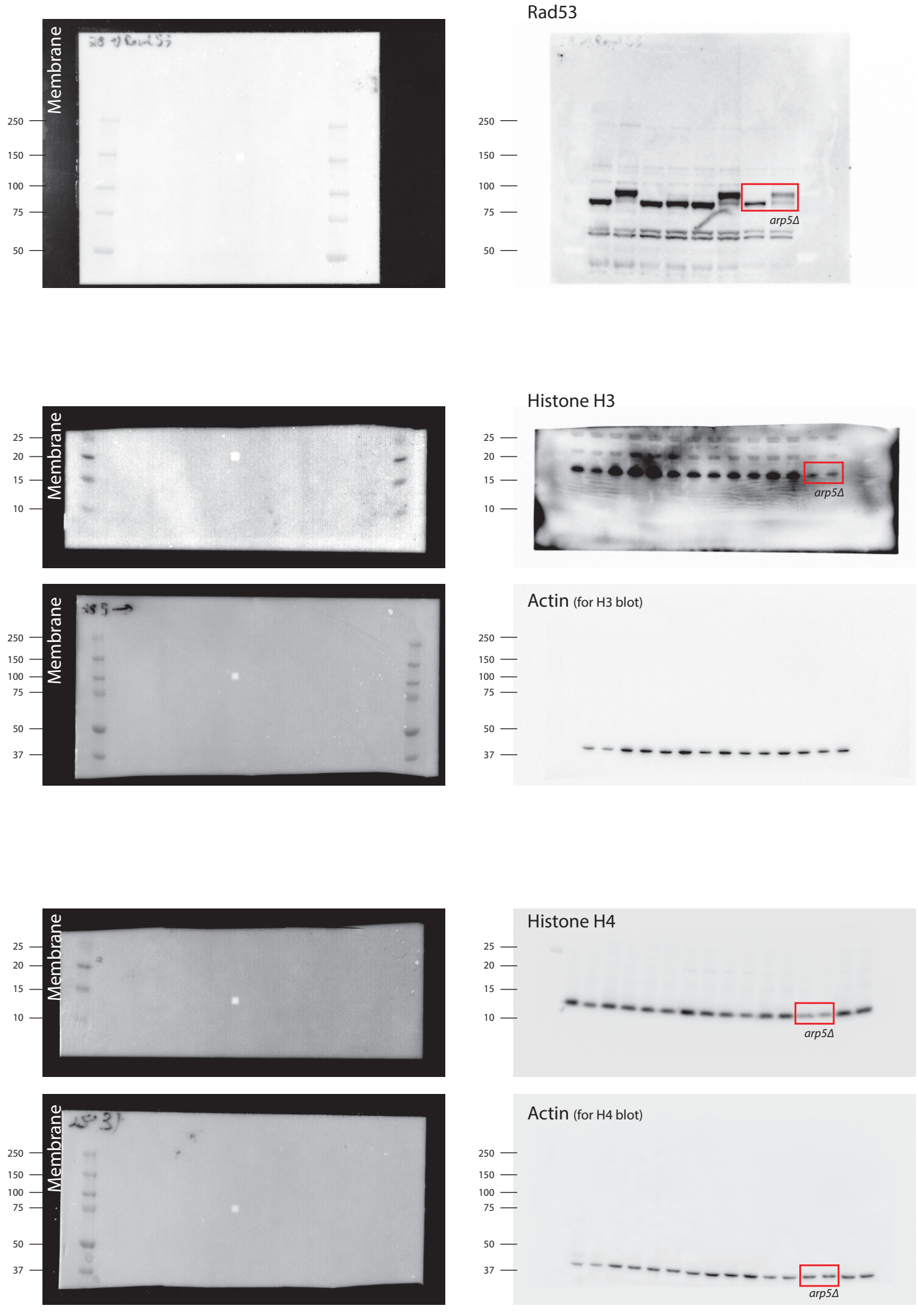
Membrane
250
150
100
75
50
Rad53
arp5Δ
Membrane
25
20
15
10
Histone H3
arp5Δ
Membrane
250
150
100
75
50
37
Actin (for H3 blot)
Membrane
25
20
15
10
Histone H4
arp5Δ
Membrane
250
150
100
75
50
37
Actin (for H4 blot)
arp5Δ